Supporting Information

Unveiling the Oxygen Adsorption Potential of ZIFs: Investigating the Impact of Ligands, Metal Centres, and Synthesis Methods

Hamidreza Mahdavi,*[a,b] Leena Melag,[c] Abdollah Khosravanian,[a] Joydip Mondal,[c] Zongli Xie,*[b] Benny D. Freeman,*[a,d] Matthew R. Hill,*[e]

[a] Department of Chemical and Biological Engineering, Monash University, Clayton, VIC 3800, Australia.

[b] CSIRO, Manufacturing, Private Bag 10, Clayton South, VIC 3169, Australia.

[c] CSIRO, Mineral Resources, Private Bag 10, Clayton South, VIC 3169, Australia.

[d] John J. McKetta Jr. Department of Chemical Engineering, The University of Texas at Austin, 2501 Speedway, Austin, TX, 78712, USA.

[e] Department of Materials Science and Engineering, Monash University, Clayton, VIC 3800, Australia.

S1: Chemicals

All reagents, including zinc nitrate hexahydrate ($Zn(NO_3)_2 \cdot 6H_2O$, 98%), iron(II) sulfate heptahydrate ($FeSO_4 \cdot 7H_2O$, 99%), cobalt(II) nitrate hexahydrate ($Co(NO_3)_2 \cdot 6H_2O$, 98%), imidazole (IM, 99%), 2-methylimidazole (mIM, 99%), and benzimidazole (bIM, 98%) as well as solvents such as dimethylformamide (DMF, 99.8%), anhydrous DMF (99.8%), and methanol (MeOH, 99.8%) were supplied from Sigma-Aldrich and were used as supplied.

S2: Synthesis methods

Magnetic Stirring (MS)

Pure and bimetallic ZIF-7 were synthesised by dissolving 20 mmol metal salts in 1000 mL of DMF. For pure ZIF-7, 20 mmol of $Zn(NO_3)_2 \cdot 6H_2O$ was used while for bimetallic ZIF-7, 20 mmol mixed-metals solution with a $Zn(NO_3)_2 \cdot 6H_2O$ to $FeSO_4 \cdot 7H_2O$ or $Co(NO_3)_2 \cdot 6H_2O$ molar ratio of 90:10 was prepared. Subsequently, a ligand solution was prepared by dissolving 130 mmol of bIM in 1000 mL of DMF. A milky solution containing precipitated nanoparticles was produced by rapidly pouring the metal salt solution into the ligand solution. The reaction was completed by strong magnetic stirring (MS) at 500 rpm and ambient temperature for 24 h. The product was collected with centrifugation, and then washed with DMF and MeOH in order, with each wash being performed at least three times. Finally, it was dried under vacuum at 120 °C for 12 h.[1]

ZIF-8, its associated Co bimetallic structures, and the Zn/Fe-mIM series (ZIF-8 (Zn:Fe = 90:10) and ZIF-8-derived Zn/Fe-mIM materials for Zn:Fe = 75:25-0:100) were synthesised by dissolving 50 mmol metal salts in 1000 mL of MeOH. For pure ZIF-8, 50 mmol $Zn(NO_3)_2 \cdot 6H_2O$ was used, whereas for others, a 50 mmol mixed-metal solution was prepared by dissolving x mmol of $Zn(NO_3)_2 \cdot 6H_2O$ and xx mmol of $FeSO_4 \cdot 7H_2O$ or $Co(NO_3)_2 \cdot 6H_2O$ in 1000 mL of MeOH. The mol.% of x to xx were adjusted to 90:10, 75:25, 50:50, 25:75, and 0:100, depending on the desired composition. Then, 400 mmol mIM was dissolved in 1000 mL

of MeOH to prepare the ligand solution. Finally, by quickly pouring the metal salt solution into the solution of ligand under MS, the mixture gradually becomes turbid after 1 h of stirring at 500 rpm, indicating the formation of nanoparticles, which were then separated from the mixture. The product was dried in a vacuum oven at 120 °C for 12 h after centrifugation and washing with MeOH at least three times.[2]

Pure and bimetallic ZIF-62 were synthesised via solvothermal treatment in a Teflon-lined autoclave. 6.98 mmol of metal salts was dissolved in 150 mL of anhydrous DMF. For pure ZIF-62, 6.98 mmol of $Zn(NO_3)_2 \cdot 6H_2O$ was used and for bimetallic ZIF-62, a 6.98 mmol mixed-metals solution was prepared by dissolving $Zn(NO_3)_2 \cdot 6H_2O$ and $FeSO_4 \cdot 7H_2O$ or $Co(NO_3)_2 \cdot 6H_2O$ with a molar ratio of 90:10. Subsequently, 94.19 mmol of IM and 10.46 mmol of bIM were prepared. The solutions were initially mixed with MS at 500 rpm for 1 h to ensure homogeneity. The resulting mixture was transferred to a 150 mL Teflon-lined autoclave, which was subsequently placed in an oven at 120 °C for 96 h. Thereafter, the autoclave was allowed to cool to room temperature. The product was collected with centrifugation, and washed with DMF and MeOH, each a minimum of three times. It was then dried in a vacuum oven at 120 °C for 12 h.[3]

Overhead Stirring (OS)

The synthesis using OS followed a procedure similar to the MS method, with the main difference being the agitation mode. To ensure consistency, the same precursor stoichiometry and post-synthesis washing/drying conditions as in the MS method. A CSIRO-developed SWIRLFLOW® stirrer that generates a tornado-like vortex and facilitates the mechanical mixing process was used for the agitation process of the premixed precursors. The mixing for the present experiment was mainly adjusted by the agitator's rotational speed and the D/T ratio (the ratio of blade diameter to tank diameter = 0.2817). This results in a blade tip velocity of approximately 0.46 $m.s^{-1}$, which induces liquid motion throughout the mixing tank. For ZIF-8

or ZIF-8 (Zn:Co = 90:10), the metal salt solution and ligand solution were mixed with OS at 500 rpm for 1 h. For ZIF-62 or ZIF-62 (Zn:Fe = 90:10), the initial mixing of both solutions was performed with OS at 500 rpm for 1 h before the solvothermal synthesis.

Ultrasonication (US)

The synthesis using US followed a procedure similar to the MS method, with the main difference being the agitation method. The reactions were performed using an ultrasonic antifouling device called CleanAHull, which produced sound waves of frequency (19 to 70 kHz) into the liquid solvent. The system uses a 44 mm diameter transducer that auto-calibrates prior to operation and then emits targeted ultrasonic bursts; following self-calibration, the transducer delivers up to 50 W peak power. In this method, the metal salt solution was added to the ligand solution while subjected to ultrasonic agitation at a frequency of 40 kHz for 1 h to synthesise ZIF-8 or ZIF-8 (Zn:Co = 90:10). Similarly, ultrasonic treatment was applied to ZIF-62 or ZIF-62 (Zn:Fe = 90:10) for 1 h as initial mixing before transferring the mixture to an autoclave for solvothermal synthesis.

Combination of Overhead Stirring and Ultrasonication (OS & US)

The synthesis using OS & US followed a procedure similar to the MS method, with the main difference being the simultaneous application of OS and US during mixing. This combination of methods uses the advantages of both the OS and US methods. The premixed precursor solution is subjected to the combined effects of mechanical stirring and acoustic forces. This may affect the consistent flow distribution provided by the independent operation of the stirrer or the ultrasound. The intense stirring forces of the stirrer may randomly disperse the bubbles, resulting in a nonuniform distribution of cavitation locations throughout the liquid. The ZIF-8 or ZIF-8 (Zn:Co = 90:10) solutions were mixed with the OS at 500 rpm for 1 h while simultaneously undergoing ultrasonic agitation at a frequency of 40 kHz. The ZIF-62 or ZIF-62 (Zn:Fe = 90:10) solutions underwent the same 1 h OS and US combination for initial mixing

right before being transferred to an autoclave for thermal treatment under similar conditions to the MS method.

Ball Milling (BM)

Ball milling (BM) offered a solvent-free method for the synthesis of ZIFs.[4, 5] The precursor stoichiometry and post-synthesis washing/drying were kept consistent with the MS method unless otherwise stated. Mechanochemical reactions were carried out using a SPEX 8000-series mill. Under the 230 V / 50 Hz configuration, the clamp operates at 1080 back-and-forth cycles.min^{-1} (cpm). Reactions were performed in a 45 mL milling jar charged with the solid precursors and 8 mm hardened-steel balls (30 balls; total ball mass ≈ 50 g). Milling was conducted for 30 min at ambient temperature. For ZIF-8, 2.00 mmol $Zn(NO_3)_2 \cdot 6H_2O$ and 16.00 mmol mIM were combined as powders and milled under the conditions above. For ZIF-8 (Zn:Co = 90:10), 1.80 mmol $Zn(NO_3)_2 \cdot 6H_2O$ and 0.20 mmol $Co(NO_3)_2 \cdot 6H_2O$ were milled with 16.00 mmol mIM. The milled powders were separated from the grinding media. For ZIF-62, 1.00 mmol $Zn(NO_3)_2 \cdot 6H_2O$ was milled with 13.49 mmol IM and 1.50 mmol bIM. For ZIF-62 (Zn:Fe = 90:10), 0.90 mmol $Zn(NO_3)_2 \cdot 6H_2O$ and 0.10 mmol $FeSO_4 \cdot 7H_2O$ were milled with 13.49 mmol IM and 1.50 mmol bIM. After milling, the product was separated from the balls, collected, and transferred to the subsequent thermal treatment phase**.**

Microwave (MW)

Microwave (MW) irradiation accelerated the ZIFs synthesis. The precursor solutions were prepared as described for the MS method, but the mixture was subjected to MW irradiation as the energy input. The microwave synthesis was carried out using a Biotage Initiator^{+} single-mode microwave reactor (2.45 GHz magnetron; power range 0-400 W; rated up to 300 °C and 30 bar). Reactions were carried out in sealed 20 mL MW vials charged with 10 mL of reaction mixture, fitted with a magnetic stir bar. The instrument was operated in temperature-controlled mode with the maximum MW power capped at 400 W; during each run the software

automatically modulated the delivered power (0-400 W) to reach and maintain the set temperature. Reaction parameters were recorded using the instrument interface program to ensure that pressure stayed within acceptable limits and temperature was maintained consistently throughout the experiment. For ZIF-8 and ZIF-8 (Zn:Co = 90:10), the precursor solutions were combined and the resulting mixture was transferred to the vial. Then it was irradiated at 120 °C for 15 min. For ZIF-62 or ZIF-62 (Zn:Fe = 90:10), the precursor mixture was similarly irradiated at 120 °C for 15 min as a pre-nucleation step before being transferred to an autoclave for solvothermal synthesis.

S3: Powder X-ray diffraction (PXRD)

The PXRD pattern was produced using a Bruker D8 Advance A25 X-ray diffractometer employing Cu Kα radiation (λ=1.54056 Å, 40 kV, 40 mA) and a Lynx Eye XE-T detector. Data was gathered from 5° to 85° with a step increment of 0.02° and a count rate of 1.6 seconds per step, while the samples were spun at 15 rpm throughout the data collection. **Figure S1** displays the PXRD patterns of ZIF-7, ZIF-8, ZIF-62, and their corresponding bimetallic derivatives containing cobalt (Co) and iron (Fe). Each series exhibits specific structural features and crystallinity. The standard patterns are derived from crystallographic information files (CIFs) obtained from the Cambridge Structural Database (CSD) and are provided for comparison with the experimentally collected PXRD data.

Figure S1a shows that ZIF-8 and its Co bimetallic versions exhibit distinct, sharp peaks, reflecting excellent crystallinity.[6] The gradual incorporation of Zn with Co results in small changes in peak positions and variations in intensities, indicating modifications in lattice characteristics attributable to the differing ionic radii of Zn and Co. Despite these changes, the structural integrity and phase purity of ZIF-8 are consistently preserved throughout the series.

Figure S1b highlights that the Zn/Fe-mIM series exhibits a trend of decreasing crystallinity as the Fe concentration increases, with Fe-rich compositions showing substantial loss of ZIF-8

long-range order. Increased Fe concentrations result in significant peak broadening and decreased intensity in the PXRD patterns, indicating reduced crystallinity/increased structural disorder. This indicates that Fe incorporation compromises framework stability, probably owing to variations in coordination preferences and ionic size compared to Zn.

Figure S1c illustrates that the PXRD patterns of ZIF-7 and its bimetallic variations exhibit the distinctive peaks of the standard ZIF-7 framework,[7] although with slightly reduced crystallinity. This is likely because ZIF-7 was produced by room-temperature rapid precipitation in coordinating DMF (immediate nanoparticle formation upon rapid mixing and no solvothermal ageing), which favours smaller coherent scattering domains and higher microstrain/defect density, leading to peak broadening and reduced intensities. The incorporation of transition metals slightly changes the diffraction patterns, indicating minor structural changes while preserving the overall ZIF-7 structure.

Figure S1d demonstrates that ZIF-62 and its bimetallic derivatives exhibit PXRD patterns that align with the standard ZIF-62 framework, hence showing successful synthesis and high crystallinity.[8] The diffraction patterns demonstrate that the addition of Co and Fe does not significantly change the framework structure, while minor peak broadening and intensity variations indicate slight changes in local ordering (e.g., coherent domain size) and/or microstrain/defect content.

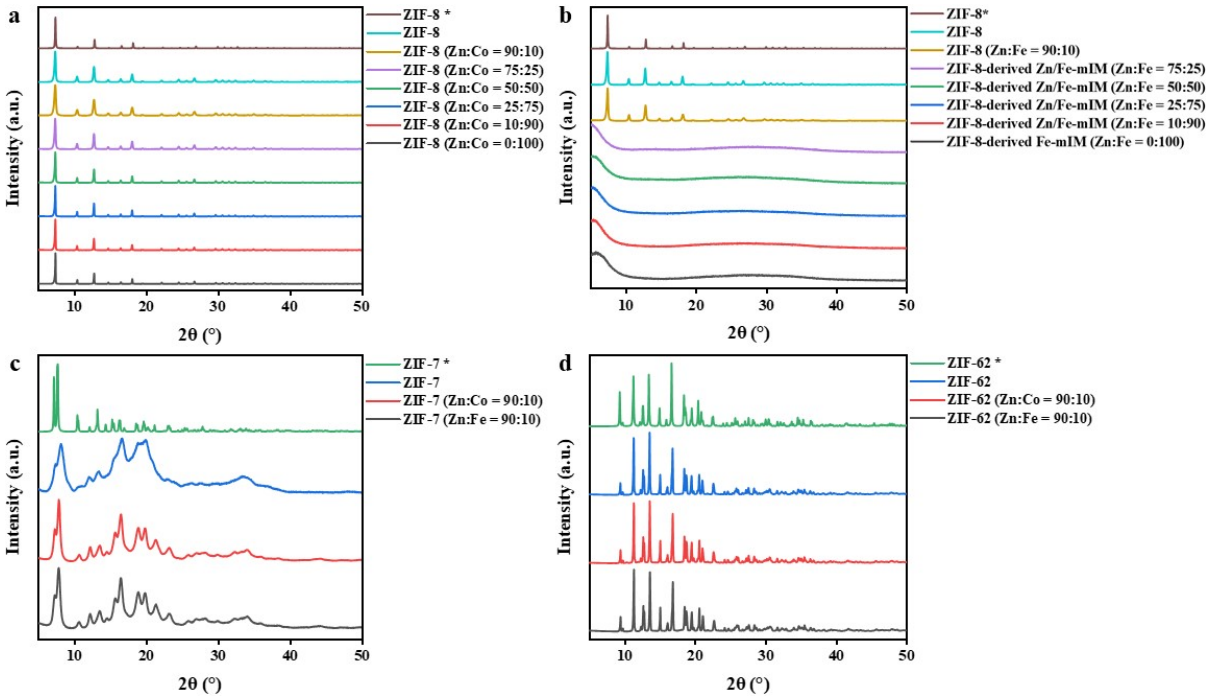

Figure S1. The PXRD patterns of a) ZIF-8 and its associated Co bimetallic structures, b) ZIF-8 and the Zn/Fe-mIM series (ZIF-8 (Zn:Fe = 90:10) and ZIF-8-derived Zn/Fe-mIM materials for Zn:Fe = 75:25-0:100), c) ZIF-7 and its associated Co and Fe bimetallic structures, and d) ZIF-62 and its associated Co and Fe bimetallic structures, synthesised using the MS method (* represents standard pattern).

Figure S2 displays the PXRD patterns of ZIF-8, ZIF-62, and their bimetallic derivatives synthesised by six different methods. The data illustrate that the selection of the synthesis method significantly affects the structural and crystallographic properties of ZIFs.

Figure S2a shows that the PXRD patterns of ZIF-8 synthesised using OS, US, and OS & US methods have similar trends to those produced by the MS method. The distinctive peaks of ZIF-8 are maintained, indicating effective framework synthesis. However, some peak broadening and decreased intensity are seen, consistent with reduced long-range order (smaller coherent scattering domains) and/or increased microstrain/defect content, i.e. a minor loss in crystallinity compared to the MS method. The BM method also displays the distinctive peaks of ZIF-8, along with additional peaks that suggest the presence of secondary phases or

impurities. These probably result from the mechanical energy imparted during BM, which might compromise the framework or generate unwanted by-products. On the other hand, the MW method replicates the ZIF-8 peaks seen in the MS method, preserving structural integrity but exhibiting significant intensity fluctuations, consistent with preferred orientation and/or differences in crystalline ordering that may arise from rapid heating and fast nucleation/growth under MW conditions.

Figure S2b presents the PXRD patterns for ZIF-8 (Zn:Co = 90:10) synthesised by the OS, US, OS & US, and MW methods, which exhibit patterns similar to the MS method, hence demonstrating the effective preservation of the bimetallic ZIF-8 framework. In the OS, US, and OS & US methods, considerable fluctuations in intensity at about 12° 2θ indicate preferential growth along certain crystallographic planes or changes in crystal orientation.

The observed peak broadening in these samples is consistent with reduced coherent domain size and/or increased microstrain/defect density, rather than being treated as a quantitative size measurement. The BM method causes additional peaks in addition to those of ZIF-8, suggesting the presence of impurity phases or secondary structures possibly resulting from the elevated mechanical energy during synthesis. This energy can lead to defects, dislocations, or partial amorphisation, leading to the observed additional peaks. Minor fluctuations in intensity, especially within the 2θ range of 10°-20°, are seen for the MW method. This suggests that, despite rapid heating, Co incorporation may help stabilise nucleation/growth, supporting comparatively uniform ordering within the bimetallic framework.

Figure S2c exhibits the PXRD patterns of ZIF-62 synthesised via OS, US, and OS & US methods, which exhibit specific ZIF-62 peaks similar to those of the MS method, but with some broadening and reduced intensities, consistent with smaller coherent domains and/or increased structural disorder/microstrain. The MW method preserves the structural framework while exhibiting variations in intensity, suggesting differences in crystallinity or crystal orientation.

The changes may be ascribed to fast nucleation and growth during the MW method. The BM method provides additional peaks in addition to those of ZIF-62, indicating the presence of secondary phases or contaminants within the ZIF-62 framework. This indicates partial framework deterioration or incomplete formation due to the high mechanical energy of BM.

Figure S2d illustrates the PXRD patterns for ZIF-62 (Zn:Fe = 90:10) synthesised by OS, US, and OS & US methods, which preserve peaks that are characteristic of the bimetallic ZIF-62 framework seen in the MS method, hence confirming structural integrity. Significant variations at about 12° 2θ in OS, US, and OS & US methods imply preferential growth or changes in orientation, while peak broadening indicates reduced long-range order (smaller coherent domains) and/or increased defect/strain content. The BM method exhibits a pattern similar to the MS method, although with extra peaks indicative of impurity phases or secondary structures. The high mechanical energy disturbs the framework's long-range order, generates defects, and facilitates by-product formation and/or secondary phases, as seen by the broadening and decreased intensity of the peaks. Minor intensity fluctuations in samples produced by the MW method in the 10°-20° 2θ range indicate changes in crystallinity or structural ordering. The observed changes are likely due to accelerated crystal growth kinetics during the MW method, driven by the presence of Fe as a stabilising secondary metal, which facilitates controlled nucleation and uniform framework formation.

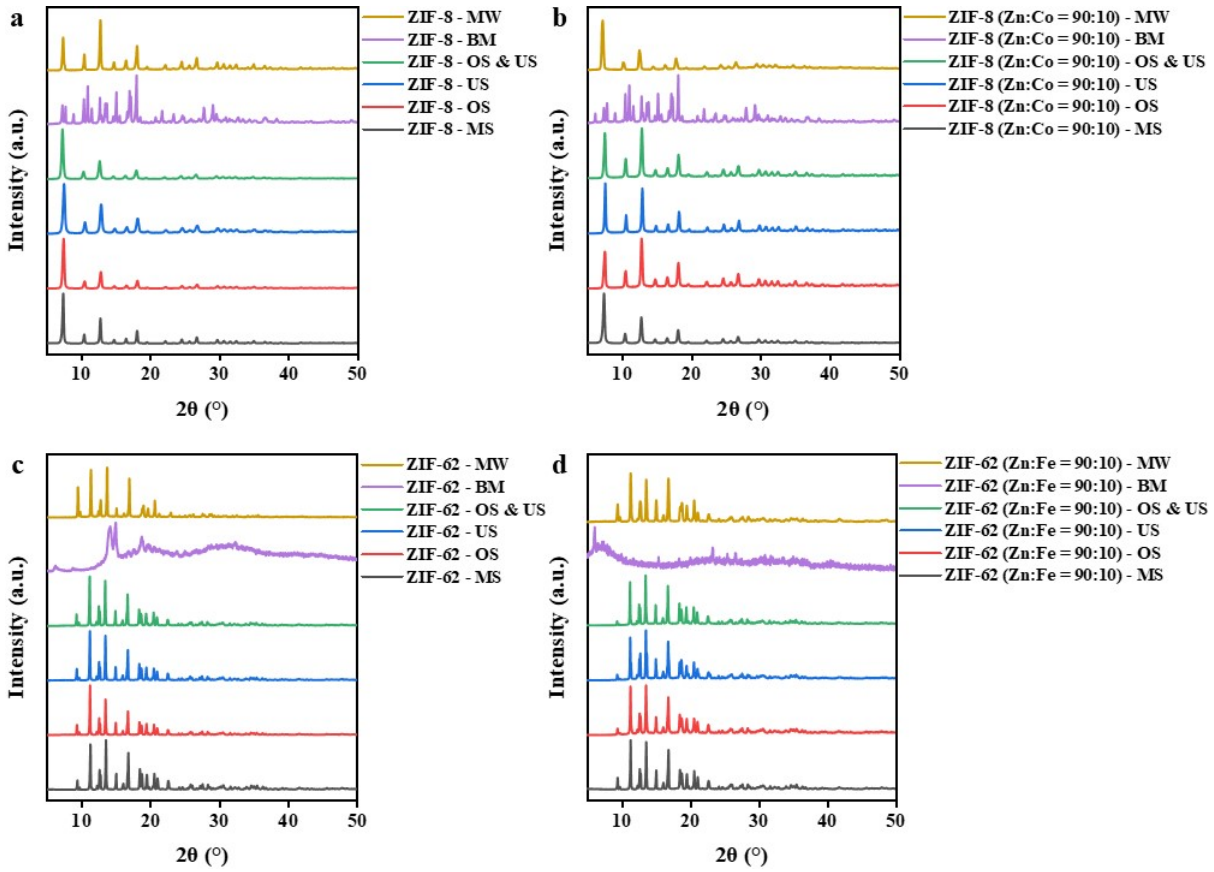

Figure S2. The PXRD patterns of a) ZIF-8, b) ZIF-8 (Zn:Co = 90:10), c) ZIF-62, and d) ZIF-62 (Zn:Fe = 90:10), synthesised using the MS, OS, US, OS & US, BM, and MW methods.

S4: Fourier-transform infrared spectroscopy (FTIR)

The FTIR spectra for each sample were collected using a Thermo Scientific Nicolet 6700 FT-IR. **Figure S3** presents FTIR spectral data used to evaluate retention of characteristic ligand functional groups and the local metal-ligand coordination environment for ZIF-7, ZIF-8, ZIF-62, and their respective bimetallic derivatives including Co and Fe.

In **Figure S3a**, the FTIR spectrum of ZIF-8 has a significant peak at 1606 cm^{-1}, indicative of the C=C stretching vibrations inside the IM ring. Peaks between 1100 cm^{-1} and 1400 cm^{-1} correspond to C-N stretching vibrations, while those in the 900-1350 cm^{-1} range refer to in-plane bending of the IM ring. A peak at 693 cm^{-1} indicates out-of-plane C-N bending, whereas the Zn-N stretching band is seen at 421 cm^{-1}, confirming the metal-ligand coordination environment.[9] The incorporation of Zn with Co in ZIF-8 induces minor changes in these peaks

(Co-N at 423 cm^{-1}), indicating changes in the bonding environment while preserving the characteristic ligand vibrations and metal-ligand coordination bands of ZIF-8.

In **Figure S3b**, ZIF-8 with increased Fe concentration has similar peaks for the IM ring (e.g., 1606 cm^{-1}, 1100-1400 cm^{-1}, 900-1350 cm^{-1}), suggesting that the characteristic ligand vibrations and metal-ligand coordination bands are maintained at lower Fe concentrations. As the Fe concentration increases, some peaks (e.g., 693 cm^{-1} and 421 cm^{-1}) decrease in sharpness or broaden, indicating a more heterogeneous local metal-ligand coordination environment and/or increased local disorder with Fe incorporation. Consistent with PXRD data, which show reduced crystallinity at higher Fe concentration, while FTIR reflects increased local coordination heterogeneity.

In **Figure S3c**, the FTIR spectrum of ZIF-7 exhibits peaks at 1455 cm^{-1} and 739 cm^{-1}, indicative of the C=C and C-H bonds in the benzene group of bIM, therefore confirming the existence of aromatic functionalities. The peaks at 1471 cm^{-1} and 1610 cm^{-1} correspond to the C-C stretching vibrations inside the aromatic ring of bIM. The peaks in the range of 600-1500 cm^{-1} are associated with bIM ring stretching and bending, consistent with retention of the bIM ligand vibrations and local bonding environment characteristic of ZIF-7.[10] The introduction of Co and Fe into ZIF-7 results in a slight shift of these distinctive peaks, indicating minor changes in the local bonding environment caused by the interaction of transition metals with the framework's ligands.

In **Figure S3d**, the FTIR spectra of ZIF-62 exhibits peaks at 1464 cm^{-1} and 745 cm^{-1}, indicative of the C=C and C-H bonds in the benzene group of bIM, similar to ZIF-7. The existence of both bIM and IM functional groups is confirmed by further peaks at 668 cm^{-1} (IM vibrations), 958 cm^{-1} (C-H out-of-plane bending of bIM), and 1070 cm^{-1} (C-H out-of-plane bending of IM).[11] The bimetallic derivatives of ZIF-62 show minor shifts in these peaks relative to the

parent ZIF-62, ascribed to changes in the force constant resulting from metal incorporation and the mixed ligand structure.

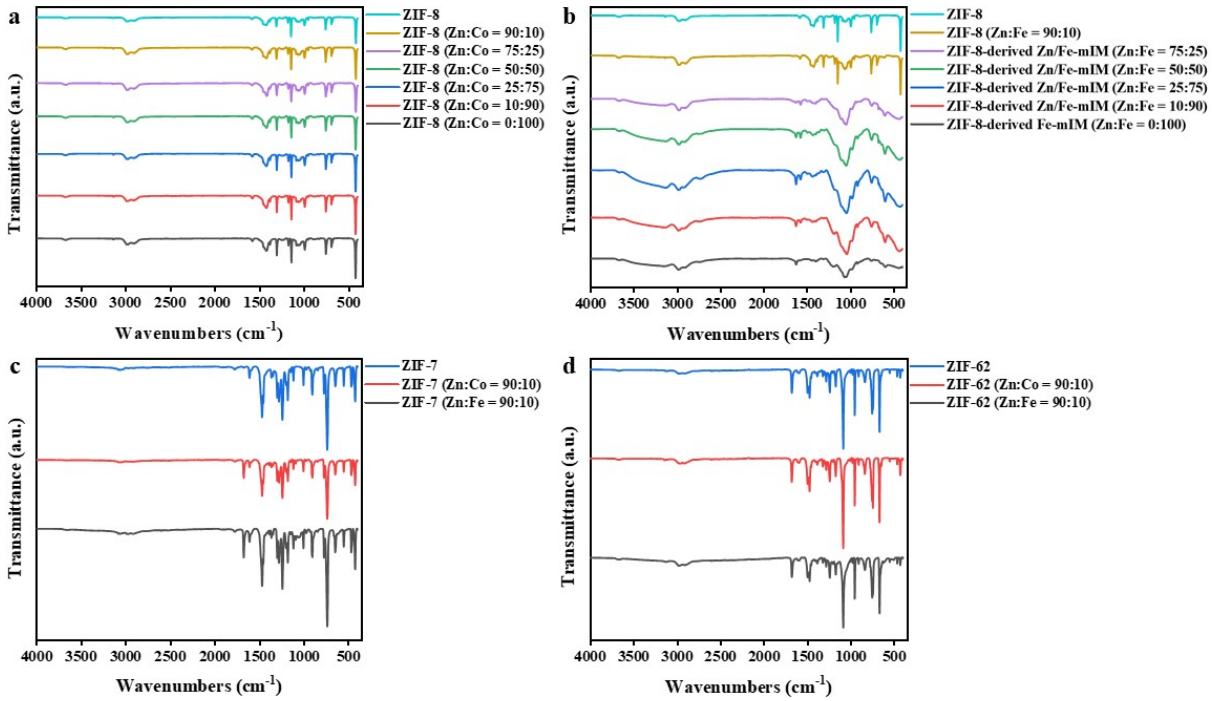

Figure S3. The FTIR spectra of a) ZIF-8 and its associated Co bimetallic structures, b) ZIF-8 and the Zn/Fe-mIM series (ZIF-8 (Zn:Fe = 90:10) and ZIF-8-derived Zn/Fe-mIM materials for Zn:Fe = 75:25-0:100), c) ZIF-7 and its associated Co and Fe bimetallic structures, and d) ZIF-62 and its associated Co and Fe bimetallic structures, synthesised using the MS method.

Figure S4 displays the FTIR spectra of ZIF-8, ZIF-62, and their bimetallic derivatives synthesised by various synthesis methods. The data highlights the effects of the synthesis method on the bonding environment of these ZIFs.

The spectra for ZIF-8 collected via the OS, US, OS & US, and MW methods remain largely consistent compared to the MS method, suggesting that these methods can retain the characteristic ligand vibrations and metal-ligand coordination bands relative to MS, indicating broadly comparable local bonding/coordination environments. The BM method results in broader and less distinct bands, consistent with milling-induced heterogeneity in the local coordination environment and/or minor by-products.

The FTIR spectra of ZIF-8 (Zn:Co = 90:10) from the OS, US, OS & US, and MW methods exhibit distinctive peaks similar to those from the MS method, indicating that the characteristic ligand vibrations are preserved despite Co incorporation. This consistency suggests broadly comparable local bonding/coordination environments across different synthesis methods. The BM method, however, yields somewhat broader peaks, indicating a more heterogeneous local coordination environment and/or additional species introduced during milling.

The FTIR spectra for ZIF-62 obtained using the OS, US, OS & US, and MW methods are similar to those from the MS method, indicating retention of the mixed-ligand functional group signatures and comparable local coordination bands irrespective of the method used. The BM method yields slightly broader peaks, indicating slight heterogeneous coordination environment and changes in metal-ligand coordination bands. This is probably due to the mechanical stress of milling, which can introduce defects and local coordination heterogeneity and/or promote minor by-products.

For ZIF-62 (Zn:Fe = 90:10), the OS, US, OS & US, and MW methods preserve the characteristic ligand vibrations as in the MS method, exhibiting only slight changes in peak sharpness and intensity. The BM method resulted in significantly broadened peaks, indicating a heterogeneous coordination environment owing to mechanical stress.

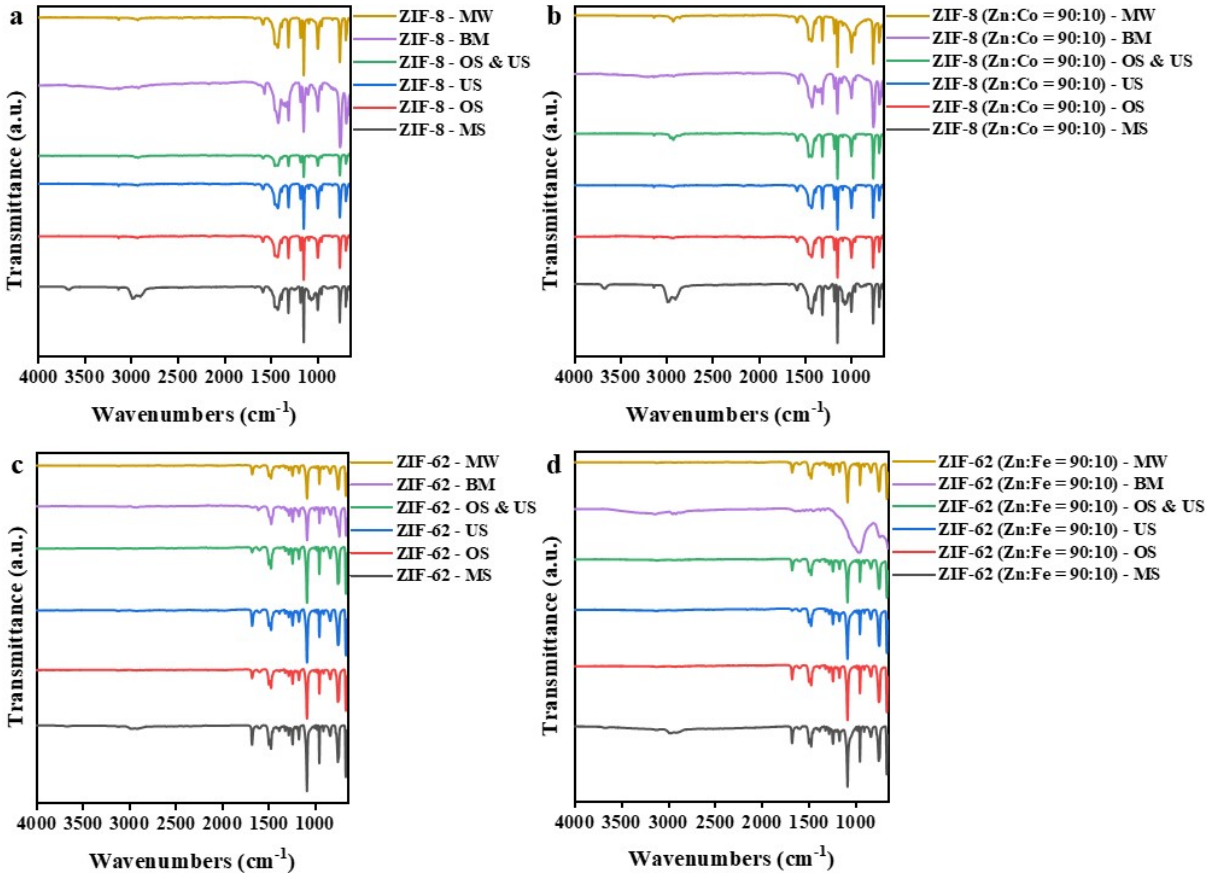

Figure S4. The FTIR spectra of a) ZIF-8, b) ZIF-8 (Zn:Co = 90:10), c) ZIF-62, and d) ZIF-62 (Zn:Fe = 90:10), synthesised using the MS, OS, US, OS & US, BM, and MW methods.

S5: Low-pressure gas sorption

The Micromeritics ASAP2420 was used to measure nitrogen (N_2) gas adsorption-desorption isotherms at 77 K (0-1 bar) using a liquid N_2 bath and ultra-high-purity gas. Brunauer-Emmett-Teller (BET) surface areas and pore size distributions (PSDs) were derived from these measurements. Materials were activated at 160 °C under dynamic vacuum for 24 h. A single activation protocol was applied to all ZIFs to enable direct comparison across compositions and synthesis methods. This condition was selected based on TGA results (Section S6), which indicate that mass loss below ~200 °C is dominated by guest/solvent removal, whereas framework degradation occurs at substantially higher temperatures. Under vacuum, desolvation is facilitated at lower temperatures, making 160 °C sufficient for activation while avoiding the risk of activation-induced collapse. BET surface areas were calculated using a

multi-point BET method in accordance with ISO 9277. Fits were performed on the adsorption branch within a relative pressure range of P/P_0 = 0.05-0.20 for all samples. In a small number of cases, the fit window was adjusted by ±1-2 points within this interval to maximise linearity while remaining within the BET-valid low-pressure region as guided by ISO 9277 (Annex B/Rouquerol consistency criteria). Apparent PSDs were calculated using an NLDFT slit-pore kernel to enable consistent comparison across the series. Given the model dependence of DFT-based PSDs, these distributions are interpreted qualitatively, particularly for samples showing hysteresis and/or low adsorption.

Figure S5 provides a comprehensive analysis of the N_2 adsorption-desorption isotherms and PSDs for ZIF-7, ZIF-8, and ZIF-62, along with their bimetallic variants, offering insights into their surface area and porosity characteristics.

The N_2 sorption isotherms for ZIF-8 and its Co bimetallic variants synthesised using the MS method have Type I behaviour, with high microporous adsorption at low pressures and minor mesoporosity, as seen by a slight hysteresis (**Figure S5a**). ZIF-8 has a BET surface area of 1401.6 $m^2.g^{-1}$, highlighting its excellent porosity (**Table S1**). PSD indicates that micropores mostly range from 10 Å to 16 Å (**Figure S5b**). The surface area increases consistently with Co incorporation, reaching a peak of 1666.7 $m^2.g^{-1}$ for ZIF-8 (Zn:Co = 0:100). This trend is attributed to the high structural tolerance of the sodalite (SOD) ZIF-8 framework toward Co^{2+} substitution, which can preserve the topology and pore network while maintaining or slightly improving accessible microporosity. The PSD shifts slightly toward ~10-15 Å with increased peak intensity which indicates a stronger and more uniform microporous domain.

For ZIF-8 and the Zn/Fe-mIM series (ZIF-8 (Zn:Fe = 90:10) and ZIF-8-derived Zn/Fe-mIM / Fe-mIM for Zn:Fe = 75:25-0:100) synthesised using the MS method, the Type I isotherm remains, with major adsorption occurring in the microporous domain (**Figure S5c**). However, increased Fe content leads to reduced adsorption capacity, greater hysteresis, and a significant

decrease in BET surface area, decreasing from 1143.0 $m^2.g^{-1}$ for ZIF-8 (Zn:Fe = 90:10) to 5.9 $m^2.g^{-1}$ for the ZIF-8-derived Fe-mIM (Zn:Fe = 0:100) (**Table S1**). This suggests the emergence of mesoporosity and amorphisation of the framework at high Fe concentrations. The incorporation of Fe leads to relatively stable PSD peaks but it significantly reduces their intensities, likely attributed to framework densification (**Figure S5d**).

The N_2 sorption isotherms for ZIF-7 and its bimetallic derivatives synthesised using the MS method exhibit Type I behaviour, with adsorption primarily found in micropores within the low-pressure range ($0 < P/P_0 < 0.01$) (**Figure S5e**). A small hysteresis at high pressures, particularly seen in the shoulder of the sorption isotherms and towards $P/P_0 = 1$, indicates minor mesoporosity attributed to structural defects. The BET surface area of ZIF-7 is 497.6 $m^2.g^{-1}$ (**Table S1**), and PSD demonstrates peaks in the microporous range of 17 Å to 27 Å (**Figure S5f**). The addition of Co and Fe slightly lowers the BET surface area. Unlike ZIF-8, ZIF-7 is more aperture-limited and sensitive to local metal-ligand geometry; substitution can more readily tighten pore windows and/or densify the local environment, which disproportionately suppresses N_2 accessibility. Consistent with this, the PSD evolves toward a single predominant peak (13 Å and 12 Å for Co and Fe, respectively), indicating a denser, more uniform microporous environment that is less accessible to N_2.

ZIF-62 and its bimetallic derivatives synthesised using the MS method also exhibit Type I isotherms, indicating adsorption mostly in the microporous area, but a small degree of mesoporosity can be identified by the small hysteresis at higher relative pressures (**Figure S5g**). ZIF-62 has a markedly lower BET surface area (193.5 $m^2 \cdot g^{-1}$) than ZIF-7 and ZIF-8 (**Table S1**), consistent with its dense mixed-ligand (IM/bIM) cag topology, which yields a more compact ultramicroporous network (PSD peaks mainly 7-10 Å; **Figure S5h**). Because this pore network is aperture-limited and close to the kinetic diameter of N_2 at 77 K, small changes in metal-ligand geometry at the nodes can disproportionately affect pore-window accessibility

and pore connectivity. Accordingly, partial substitution with secondary metal (Zn:Co or Zn:Fe = 90:10) leads to a sharp decrease in N_2-accessible surface area (193.5 to 11.6 $m^2.g^{-1}$ for Co and 193.5 to 33.5 $m^2.g^{-1}$ for Fe; **Table S1**) and reduced PSD peak intensities (**Figure S5h**), suggesting narrowing/partial occlusion of ultramicropore windows rather than a change in the overall framework topology. This heightened sensitivity of ZIF-62 to mixed-metal node incorporation is consistent with reports of structural mismatch (mixed metal node effect) in Zn/Co-ZIF-62 arising from differences in Zn-N vs Co-N bonding.[12]

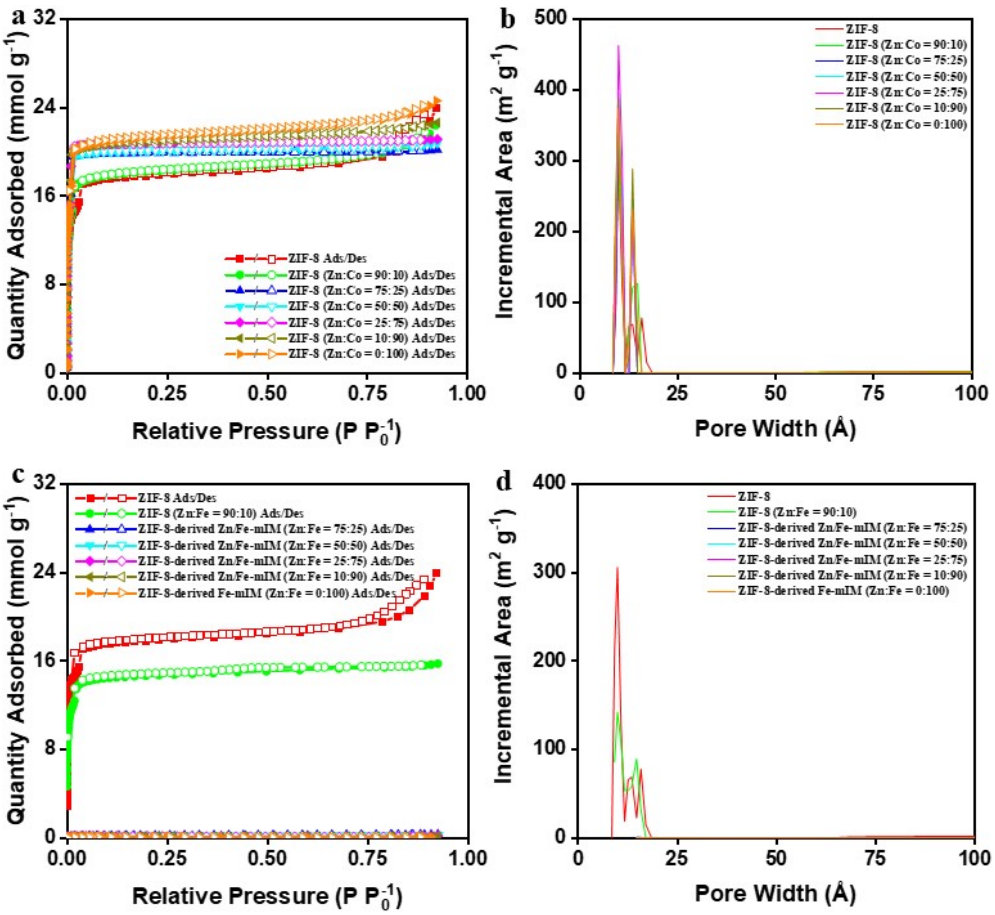

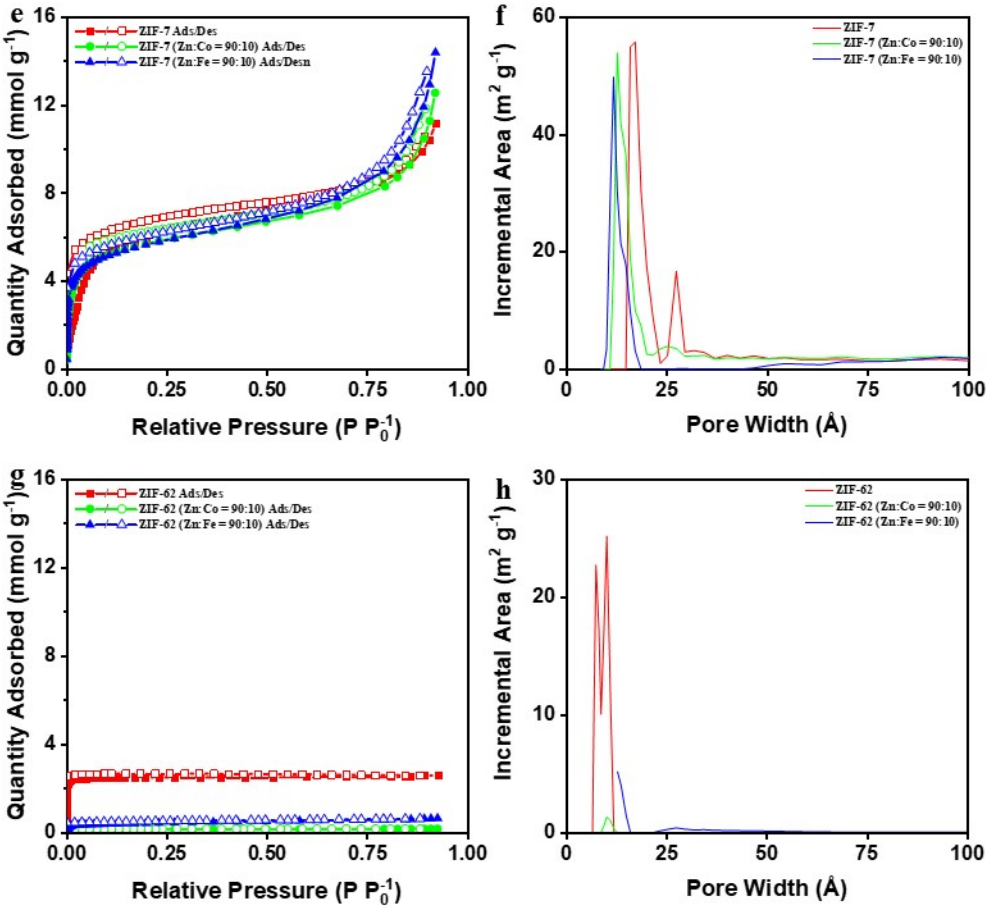

Figure S5. The N_2 adsorption isotherm and PSD of a and b) ZIF-8 and its associated Co bimetallic structures, c and d) ZIF-8 and the Zn/Fe-mIM series (ZIF-8 (Zn:Fe = 90:10) and ZIF-8-derived Zn/Fe-mIM materials for Zn:Fe = 75:25-0:100), e and f) ZIF-7 and its associated Co and Fe bimetallic structures, and g and h) ZIF-62 and its associated Co and Fe bimetallic structures, synthesised using the MS method (adsorption is represented by filled markers and desorption by unfilled markers).

Table S1. The BET and Langmuir surface areas via N_2 gas of ZIF-8, its associated Co bimetallic structures, and the Zn/Fe-mIM series (ZIF-8 (Zn:Fe = 90:10) and ZIF-8-derived Zn/Fe-mIM materials for Zn:Fe = 75:25-0:100) as well as ZIF-7, ZIF-62, and their respective bimetallic derivatives, synthesised using the MS method.

Sample	BET Surface Area ($m^2 \cdot g^{-1}$)	Langmuir Surface Area ($m^2 \cdot g^{-1}$)
ZIF-8	1402	1758
ZIF-8 (Zn:Co = 90:10)	1429	1793

ZIF-8 (Zn:Co = 75:25)	1554	1941
ZIF-8 (Zn:Co = 50:50)	1571	1964
ZIF-8 (Zn:Co = 25:75)	1622	2028
ZIF-8 (Zn:Co = 10:90)	1636	2048
ZIF-8 (Zn:Co = 0:100)	1667	2084
ZIF-8 (Zn:Fe = 90:10)	1143	1443
ZIF-8-derived Zn/Fe-mIM (Zn:Fe = 75:25)	12	15
ZIF-8-derived Zn/Fe-mIM (Zn:Fe = 50:50)	11	14
ZIF-8-derived Zn/Fe-mIM (Zn:Fe = 25:75)	8	10
ZIF-8-derived Zn/Fe-mIM (Zn:Fe = 10:90)	6	8
ZIF-8-derived Fe-mIM (Zn:Fe = 0:100)	6	8
ZIF-7	498	653
ZIF-7 (Zn:Co = 90:10)	458	587
ZIF-7 (Zn:Fe = 90:10)	453	587
ZIF-62	194	244
ZIF-62 (Zn:Co = 90:10)	12	15
ZIF-62 (Zn:Fe = 90:10)	34	43

Figure S6 provides a detailed examination of the N_2 adsorption-desorption isotherms and PSDs, while **Table S2** summarises the surface areas of ZIF-8, ZIF-8 (Zn:Co = 90:10), ZIF-62, and ZIF-62 (Zn:Fe = 90:10) synthesised using various methods.

ZIF-8s synthesised using various methods exhibit Type I isotherms, with PSD between 10 Å and 16 Å. For ZIF-8, the MS method enables uniform nucleation and controlled crystal growth, resulting in a high surface area. The OS and US methods further increase porosity, with the OS method enhancing precursor dispersion and the US method facilitating crystal dispersion while preserving microporosity. The OS & US method gives slightly higher surface area, which is consistent with a combined nucleation/dispersion effect, but the difference relative to the OS or US methods alone is small. In contrast, the BM method significantly decreases porosity due to mechanical stress-induced rapid amorphisation, densification, and framework collapse.[13] However, the MW method preserves high porosity, demonstrating that rapid nucleation can still yield a well-crystallised microporous framework.

For ZIF-8 (Zn:Co = 90:10) with similar Type I isotherms and PSD, the MS method indicates a well-defined microporous structure. The OS method increases surface area by enhancing precursor dispersion, whilst the US method further improves nucleation and porosity. The OS

& US attains a significant surface area, but somewhat less than the OS and US methods independently, suggesting that the combination effectively balances nucleation and dispersion without exceeding the efficacy of either method alone. The BM method compromises microporosity, resulting in structural collapse, whereas the MW method maintains microporosity despite rapid crystallisation.

For ZIF-62 synthesised using various methods, the isotherms also remain mainly Type I. The MS method yields the greatest porosity and surface area owing to homogeneous nucleation and regulated crystal growth. The OS and US methods create somewhat wider PSDs, with the OS method causing moderate porosity and the US method modestly improving pore accessibility, consistent with PXRD peak broadening (**Figure S2c**) suggesting smaller coherent scattering domains and/or increased structural disorder/microstrain. The OS & US method enhances nucleation and accessibility, yielding moderately porous materials with a degree of mesoporosity. The BM method modifies the pore structure by introducing defects and a microporosity with a hysteresis loop owing to mechanical stresses, while simultaneously maintaining a relatively high surface area with the fact that, in ZIF-62 synthesis, milling is followed by a thermal treatment phase that can partially recrystallise or anneal the disorder generated by milling. This suggests that porosity is redistributed rather than collapsed. The MW method is more detrimental because its mixed-ligand (IM/bIM) cag framework necessitates controlled ligand incorporation; rapid MW nucleation can obstruct proper ligand integration. Therefore, it leads to aggregation and pore blockage and producing a dense, low-porosity framework.

For ZIF-62 (Zn:Fe = 90:10) with similar Type I isotherms, the MS method demonstrates considerable porosity reduction relative to pure ZIF-62, suggesting that Fe incorporation compromises the framework, hence reducing pore accessibility. The OS and US methods enhance porosity somewhat, with the OS & US method exhibiting the greatest surface area and

well-formed microporosity. The BM method results in a significant collapse of structure, while the MW method yields the minimal surface area likely because mechanical stress under BM and rapid nucleation under MW heating, amplify mixed-metal (Zn/Fe) heterogeneity and increase susceptibility to defect formation and pore blockage and hence less N_2-accessible surface area.

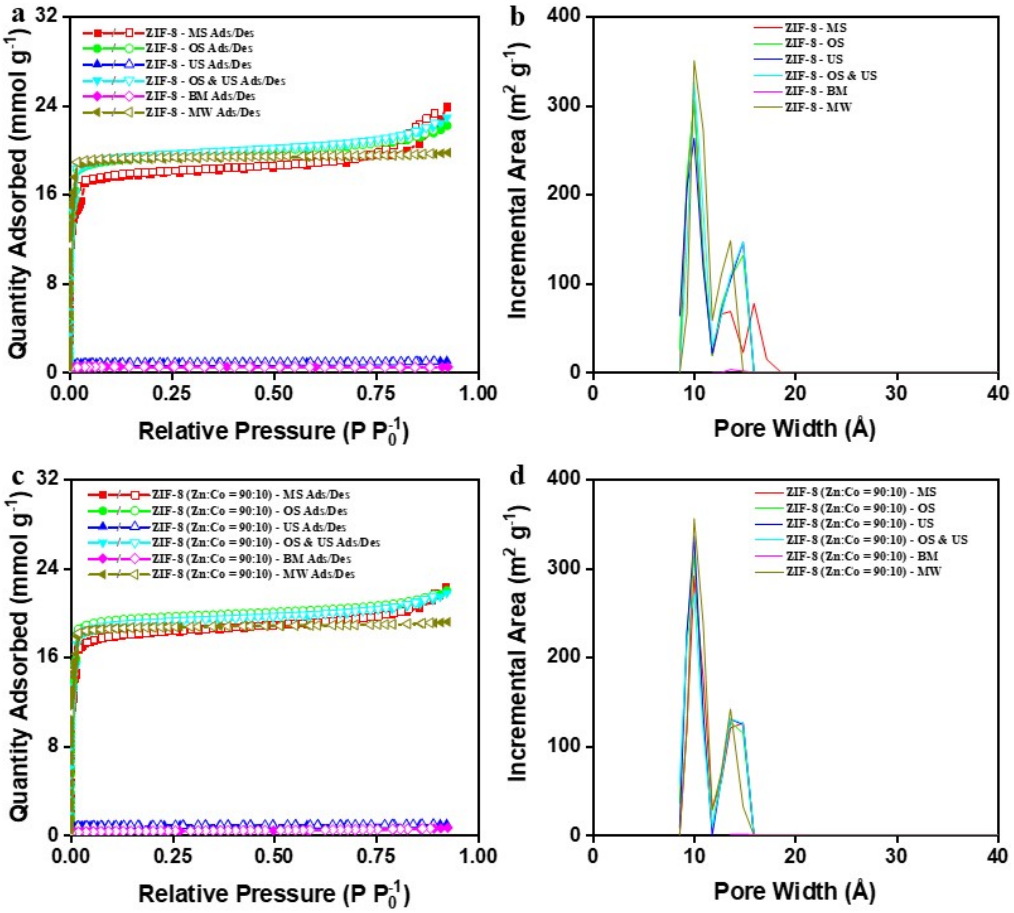

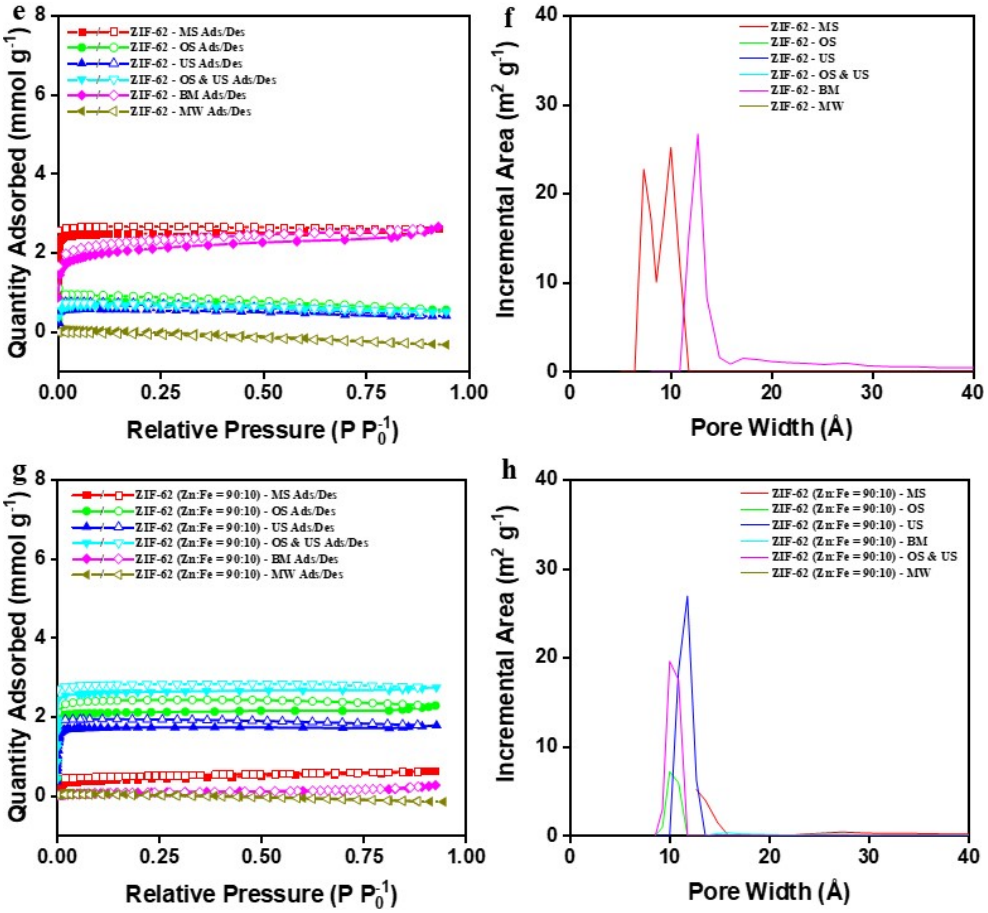

Figure S6. The N_2 adsorption isotherm and PSD of a) ZIF-8, b) ZIF-8 (Zn:Co = 90:10), c) ZIF-62, and d) ZIF-62 (Zn:Fe = 90:10), synthesised using the MS, OS, US, OS & US, BM, and MW methods (adsorption is represented by filled markers and desorption by unfilled markers).

Table S2. The BET and Langmuir surface areas via N_2 gas of ZIF-8, ZIF-8 (Zn:Co = 90:10), ZIF-62, and ZIF-62 (Zn:Fe = 90:10), synthesised using the MS, OS, US, OS & US, BM, and MW methods.

Sample	BET Surface Area ($m^2 \cdot g^{-1}$)	Langmuir Surface Area ($m^2 \cdot g^{-1}$)
ZIF-8 - MS	1402	1758
ZIF-8 - OS	1515	1899
ZIF-8 - US	1506	1889
ZIF-8 - OS & US	1528	1916
ZIF-8 - BM	40	52
ZIF-8 - MW	1501	1877
ZIF-8 (Zn:Co = 90:10) - MS	1429	1793
ZIF-8 (Zn:Co = 90:10) - OS	1528	1915
ZIF-8 (Zn:Co = 90:10) - US	1535	1924

ZIF-8 (Zn:Co = 90:10) - OS & US	1494	1872
ZIF-8 (Zn:Co = 90:10) - BM	30	38
ZIF-8 (Zn:Co = 90:10) - MW	1454	1834
ZIF-62 - MS	194	244
ZIF-62 - OS	57	73
ZIF-62 - US	43	54
ZIF-62 - OS & US	50	64
ZIF-62 - BM	164	210
ZIF-62 - MW	< 1*	< 1*
ZIF-62 (Zn:Fe = 90:10) - MS	34	43
ZIF-62 (Zn:Fe = 90:10) - OS	165	208
ZIF-62 (Zn:Fe = 90:10) - US	135	169
ZIF-62 (Zn:Fe = 90:10) - OS & US	204	258
ZIF-62 (Zn:Fe = 90:10) - BM	7	10
ZIF-62 (Zn:Fe = 90:10) - MW	3	4

* Instrument-calculated value = 0.4 $m^2.g^{-1}$

S6: Thermogravimetric analysis (TGA)

The TGA was conducted using a Mettler Toledo TGA 2 STARe System, with a heating rate of 5 °C.min^{-1} from 25 °C to 800 °C under the N_2 atmosphere. Approximately 10 mg of the material was placed into alumina crucibles. The TGA data analysis was performed with STARe Evaluation Software version 15.01 by Mettler Toledo. **Figure S7** illustrates the TGA results for ZIF-7, ZIF-8, and ZIF-62, as well as their bimetallic variants, offering an in-depth examination of their thermal stability.

The TGA data for ZIF-8 and its Co bimetallic variants synthesised using the MS method exhibit a unique thermal behaviour affected by Co concentration (**Figure S7a**). ZIF-8 shows minimal low-temperature mass loss (≈0.7 wt.% from 25-200 °C), indicating the efficient removal of methanol during the drying process. ZIF-8 shows two high-temperature mass-loss steps. The initial step at ~586 °C is attributed to decomposition of the mIM ligand and associated collapse of the ZIF-8 framework. The second step at ~773 °C occurs after framework breakdown and is ascribed to further degradation of the remaining residue (e.g., carbonaceous/metal-containing residue evolution). The residual mass at 800 °C leaves ≈34.6 wt.%. The pattern of solvent loss across all Co-substituted variants is similar to ZIF-8, with all Co variants showing comparably

low mass loss below ~250 °C (≈0.4-1.0 wt.% over 25-200 °C, depending on Co content), indicating that the addition of Co does not influence solvent retention inside the ZIF-8 framework. The residual mass at 800 °C across the Co variants, leaving ≈24.1-43.3 wt.% (composition-dependent). As the Co concentration increases, degradation temperatures initially decline, but as Co content increases, they shift back to higher temperatures, with the fully Co-substituted variant (Zn:Co = 0:100) showing relatively similar thermal stability to ZIF-8. This trend is ascribed to composition-dependent variations in framework order and the local metal-ligand environment, as demonstrated by the PXRD retention of the ZIF-8 pattern with only minor changes in peak shape and position (**Figure S1a**) and the FTIR preservation of the characteristic ligand bands with a slight shift in the metal-ligand stretching region (**Figure S3a**). The results suggest the existence of an isostructural Zn/Co series instead of the formation of a new phase.

The TGA results for ZIF-8 and the Zn/Fe-mIM series (ZIF-8 (Zn:Fe=90:10) and ZIF-8-derived Zn/Fe-mIM / Fe-mIM for Zn:Fe = 75:25-0:100) synthesised using the MS method demonstrate an opposite trend relative to the Co variants (**Figure S7b**). Fe-substituted samples show notably higher low-temperature mass loss, with approximately ~4.2 wt.% loss by ~200 °C for Zn:Fe = 90:10, increasing to roughly ~13.9 wt.% loss over a 25-200 °C range for ZIF-8-derived Fe-mIM material (Zn:Fe = 0:100). This indicates that Fe substitution increases solvent retention or strongly bound species relative to pristine ZIF-8. The residual mass at 800 °C across the Fe variants, leaves ≈34.6-41.7 wt.% (composition-dependent). As the Fe concentration increases, the degradation temperatures systematically decline, with the ZIF-8-derived Fe-mIM material (Zn:Fe = 0:100) showing decomposition onset at lower temperatures than ZIF-8. The lower thermal stability is ascribed to higher structural disorder resulting from Fe incorporation, evidenced by PXRD peak broadening and diminished intensities with increasing Fe

concentration (**Figure S1b**), as well as broadening and reduced intensity in the metal-ligand region in FTIR (**Figure S3b**), signifying a more heterogeneous local coordination environment. The TGA data of ZIF-7 and its bimetallic derivatives synthesised using the MS method indicate a two-step thermal degradation process (**Figure S7c**). ZIF-7 exhibits only minor low-temperature mass loss (~0.6 wt.% up to ~200 °C), corresponding to the evaporation of residual DMF solvent, followed by gradual mass reduction before major framework degradation. ZIF-7 also exhibits two high-temperature degradation characteristics: the ~606 °C step corresponds to bIM ligand/framework decomposition, while the ~782 °C step is attributed to further residue evolution. The mass decrease led to ≈56.3 wt.% residual mass at 800 °C. The Co- and Fe-substituted variants show higher early losses than pristine ZIF-7, with approximate mass losses of ~2.7 wt.% (Zn:Co = 90:10) and ~4.1 wt.% (Zn:Fe = 90:10) in the 25-200 °C region. For these bimetallic ZIF-7 variants, for Zn:Co = 90:10 the residual mass at 800 °C is ≈68.9 wt.% and≈55.0 wt.% residual mass at 800 °C for Zn:Fe = 90:10. This behaviour suggests increased solvent retention relative to ZIF-7 and a composition-dependent influence on the extent of high-temperature decomposition. This is possibly owing to a more compact framework structure that entraps more solvent molecules inside the pores. The degradation temperatures of the bimetallic derivatives are slightly decreased, especially for the Fe variant, indicating that metal incorporation induces relatively small structural changes that decrease thermal stability. The TGA study on ZIF-62 and its bimetallic versions synthesised using the MS method demonstrates higher thermal stability relative to ZIF-7 and ZIF-8 (**Figure S7d**). ZIF-62 shows moderate low-temperature mass loss of ~3.0 wt.% between 25-200 °C, consistent with partial retention of residual solvent species, attributed to its denser dual-ligand structure. ZIF-62 has two main degradation features, with the primary event at ~601 °C associated with IM and mIM mixed ligand and framework decomposition and a later event at ~788 °C assigned to continued residue evolution. The residual mass at 800 °C is 62.2 wt.%. The Co- and Fe-substituted

variants exhibit similar low-temperature losses of ≈3.1-3.4 wt.% up to ~200 °C for Zn:Fe = 90:10 and Zn:Co = 90:10, indicating that partial metal replacement does not significantly affect early mass loss. The residual mass at 800 °C for the Co-substituted variant is ≈58.9 wt.% and ≈44.8 wt.% for the Fe-substituted variant, indicating greater high-temperature mass loss for the Fe-containing framework. In the Co-substituted variant, the degradation temperatures remain largely unchanged, suggesting that Co incorporation hardly affects the structural integrity of the framework. The Fe-substituted variant exhibits minor reduced degradation temperatures, indicating slightly lower framework stability, probably attributable to structural distortions caused by Fe incorporation.

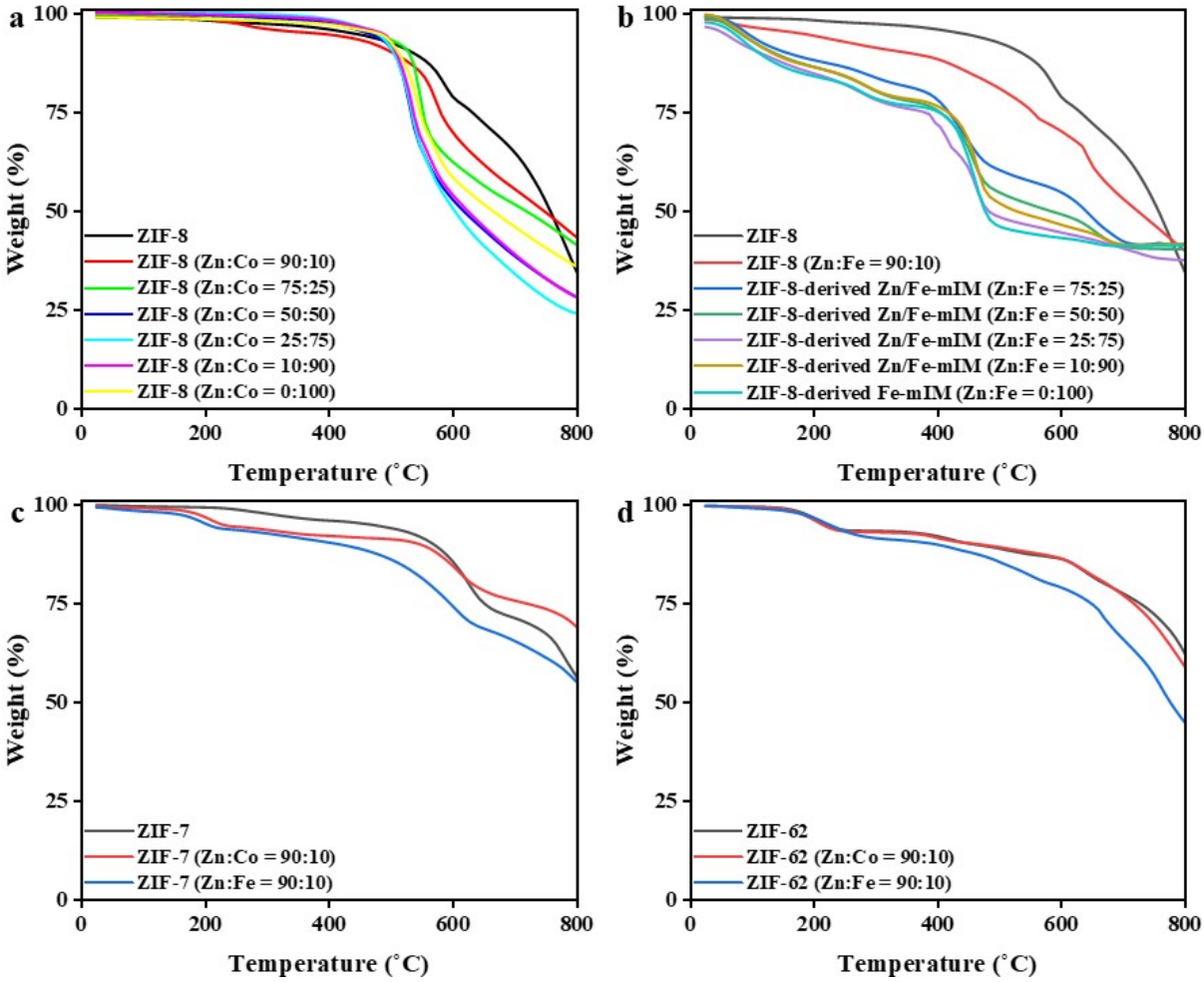

Figure S7. The TGA graphs of a) ZIF-8 and its associated Co bimetallic structures, b) ZIF-8 and the Zn/Fe-mIM series (ZIF-8 (Zn:Fe = 90:10) and ZIF-8-derived Zn/Fe-mIM materials for

Zn:Fe = 75:25-0:100), c) ZIF-7 and its associated Co and Fe bimetallic structures, and d) ZIF-62 and its associated Co and Fe bimetallic structures, synthesised using the MS method.

Figure S8 provides the TGA data of ZIF-8, ZIF-62, and their bimetallic derivatives (Zn:Co = 90:10 and Zn:Fe = 90:10, respectively) synthesised using several methods including the MS, OS, US, OS & US, BM, and MW. The findings underscore the influence of synthesis methods on the thermal stability and the decomposition characteristics.

For ZIF-8 synthesised using the OS, US, OS & US, and MW methods, mass loss remains low up to ~250 °C (≈0.2-0.4 wt.% over 25-200 °C), leaving ≈35.4-44.5 wt.% residual mass at 800 °C (method-dependent), exhibiting slightly more stability than the MS method (**Figure S8a**). However, the BM method demonstrates higher early loss (≈2.8 wt.% by 200 °C), leaving ≈39.2 wt.% residual mass at 800 °C. The higher initial loss in the BM method is primarily due to the removal of additional adsorbed or confined species (e.g., water, solvent, residual ligand, by-products) associated with a defect-rich or disordered framework as confirmed by PXRD and FTIR (**Figures S2** and **S4**) and a diminished N_2-accessible surface area (**Table S2**).

For ZIF-8 (Zn:Co = 90:10), the OS, US, OS & US, and MW methods show very low early losses (≈0.1-0.4 wt.% over 25-200 °C) (**Figure S8b**). Residual mass at 800 °C across these methods was ≈37.5-44.2 wt.% (method-dependent). However, the BM method exhibits a higher early loss (≈3.3 wt.% by 200 °C) (aligned with PXRD/FTIR evidence for disorder and porosity reduction; **Figures S2** and **S4**; **Table S2**), and results in the lowest residual mass at 800 °C (≈39.7 wt.%), indicating significantly reduced stability relative to other methods.

For ZIF-62, the OS, US, OS & US, BM, and MW methods yield low-temperature losses spanning ≈0.5-2.5 wt.% over 25-200 °C (method-dependent), leaving ≈59.6-67.7 wt.% residual mass at 800 °C (**Figure S8c**). Whereas the BM method exhibits the lowest low-temperature mass loss (≈0.4 wt.% over 25-200 °C) and the largest residue (≈70.5 wt.% at 800 °C). This

relatively minor early loss aligns with the slight change in N_2-accessible surface area found for the BM method.

For ZIF-62 (Zn:Fe = 90:10), the OS, US, OS & US, and MW methods exhibit low-temperature losses of ≈0.9-2.8 wt.% over 25-200 °C, leaving ≈45.5-64.0 wt.% residual mass at 800 °C (method-dependent) (**Figure S8d**). In contrast, the BM method gives the largest early loss (≈7.5 wt.% by 200 °C) and results in a low residue (≈46.0 wt.% at 800 °C). This behaviour aligns with the emergence of structural defects and reduced crystallinity as indicated by PXRD/FTIR evidence of disorder and porosity loss (**Figures S2** and **S4**; **Table S2**) resulting from mechanical stress during the BM method. This contrasts with monometallic ZIF-62, where the post-milling thermal treatment phase results in only slight changes in porosity; in ZIF-62 (Zn:Fe = 90:10), the presence of mixed-metal nodes and associated heterogeneity in local bonding and geometry likely increases susceptibility to mechanical stress, resulting in increased disorder and pore blockage, which in turn leads to greater initial mass loss and diminished thermal stability.

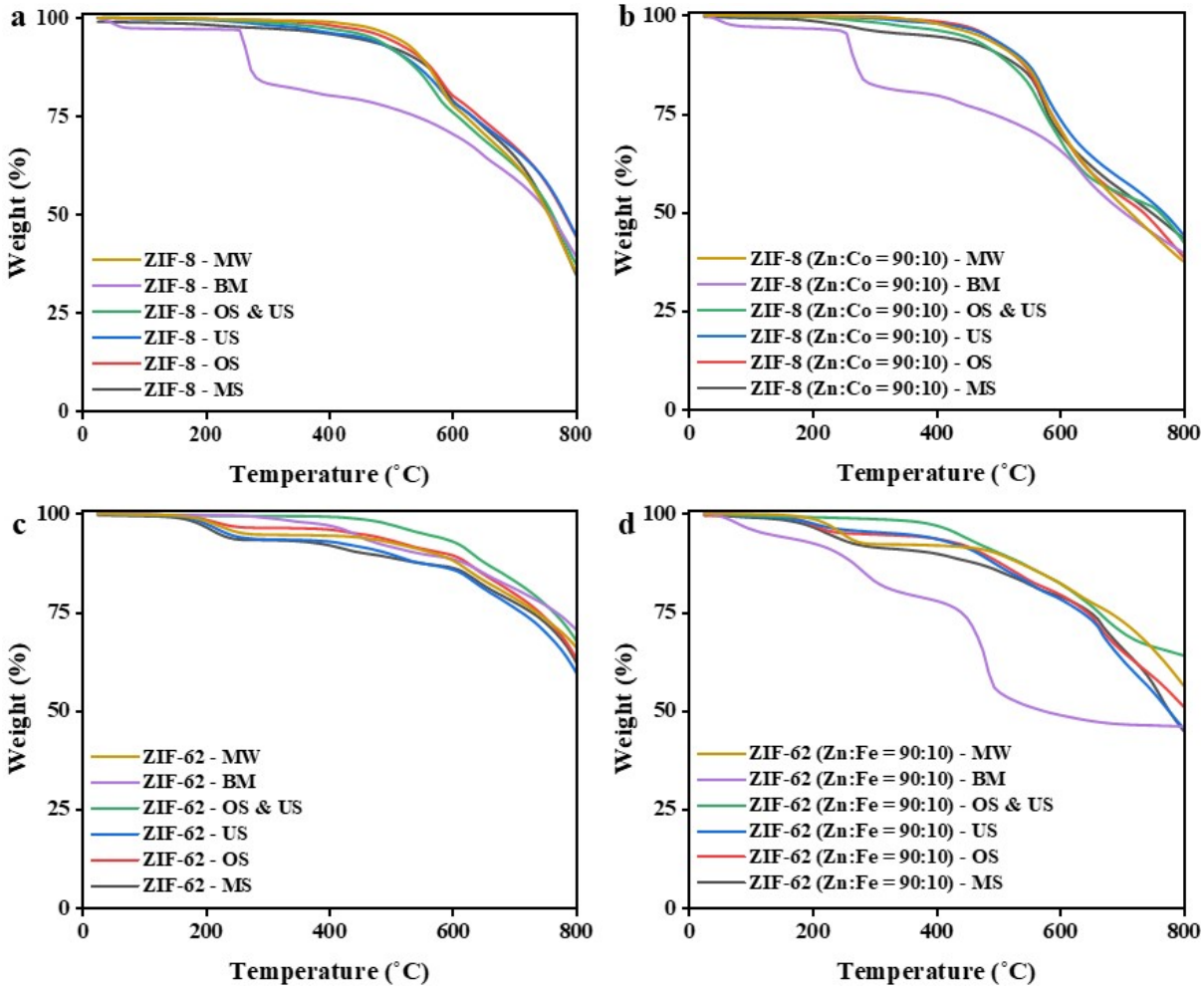

Figure S8. The TGA graphs of a) ZIF-8, b) ZIF-8 (Zn:Co = 90:10), c) ZIF-62, and d) ZIF-62 (Zn:Fe = 90:10), synthesised using the MS, OS, US, OS & US, BM, and MW methods.

S7: Scanning electron microscope (SEM)/energy-dispersive X-ray spectroscopy (EDX)

Scanning Electron Microscopy (SEM) was conducted using a Thermo Scientific Verios 5 UC FEGSEM. All samples were mounted on aluminium stubs and coated with carbon. The working distance was 4 mm, and pictures were acquired at an accelerating voltage of 5 kV and spot size of 2.

Figure S9 illustrates the SEM/EDX images results for ZIF-7, ZIF-8, and ZIF-62, as well as their bimetallic variants, offering clear visual evidence of their distinct morphology and elemental composition distribution. The SEM image of ZIF-8 displays well-defined rhombic dodecahedral crystals, characteristic of its SOD topology. These crystals have sharp edges and

flat facets, indicating a highly ordered and symmetrical structure with uniform size and form. ZIF-7 also exhibits an SOD topology; however, its shape varies owing to the incorporation of bIM as the ligand. This variation in ligand chemistry yields crystals that are often more spherical. ZIF-62, however, has a distinctive morphology influenced by its peculiar cage-like (CAG) structure, resulting from a mixed-ligand composition. SEM imaging shows irregular polyhedral crystals, exhibiting surfaces that are either smooth or wavy. This form illustrates the complex structural configuration and growth dynamics induced by the mixed ligands. EDX confirms the presence of zinc (Zn) and its consistent and uniform spatial distribution across the particles for ZIF-7, ZIF-8, and ZIF-62. The incorporation of cobalt (Co) into ZIF-8 results in particles that mostly maintain the distinctive rhombic dodecahedral morphology. This is confirmed by PXRD, which shows ZIF-8 (SOD) phase retention across the Co variants (**Figure S1a**). As the Co content rises, the particles maintain their polyhedral morphology, while a significant increase in particle size is seen. A similar retention of particle morphology is observed for ZIF-7 and ZIF-62. PXRD confirms retention of the parent phases for their bimetallic variants (**Figures S1c-S1d**). In contrast, increasing Fe content leads to progressively less faceted, more fused/aggregated particles (morphological degradation). With minor Fe content, the particles exhibit increased surface roughness and aggregation, along with a partial degradation of their well-defined polyhedral morphology. With an increase in Fe concentration, the morphology becomes more amorphous, characterised by irregular, fused particles without sharp edges, signifying significant structural instability. Similar behaviour is seen in ZIF-7 and ZIF-62, where Fe substitution induced coordination discrepancies, resulting in changed particle morphology. EDX confirms the presence and consistent and homogeneous spatial distribution of Zn together with the second metal (Co or Fe) across the particles. As the Co/Fe fraction increases, the relative Zn signal decreases accordingly.

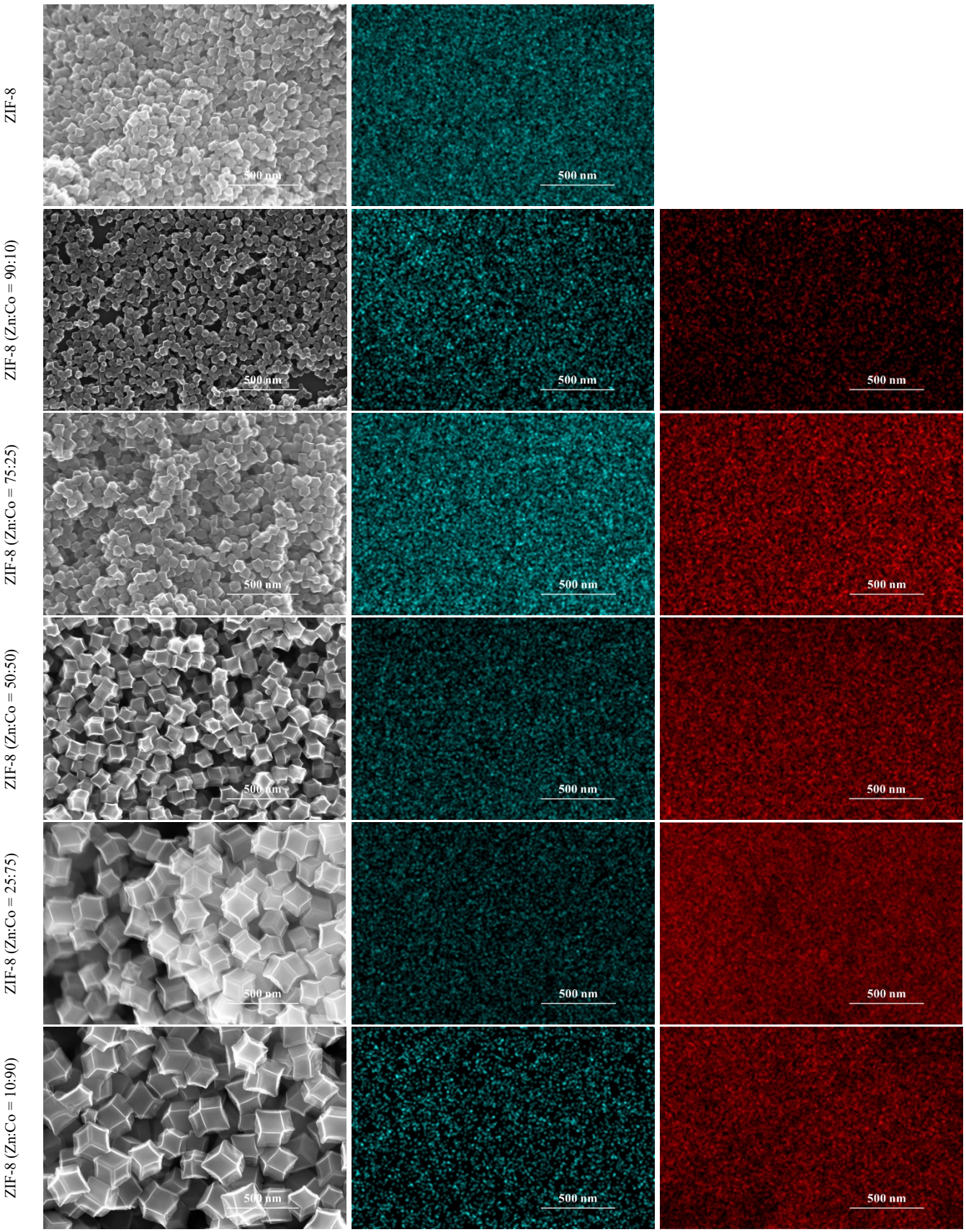
ZIF-8
ZIF-8 (Zn:Co = 90:10)
ZIF-8 (Zn:Co = 75:25)
ZIF-8 (Zn:Co = 50:50)
ZIF-8 (Zn:Co = 25:75)
ZIF-8 (Zn:Co = 10:90)
500 nm

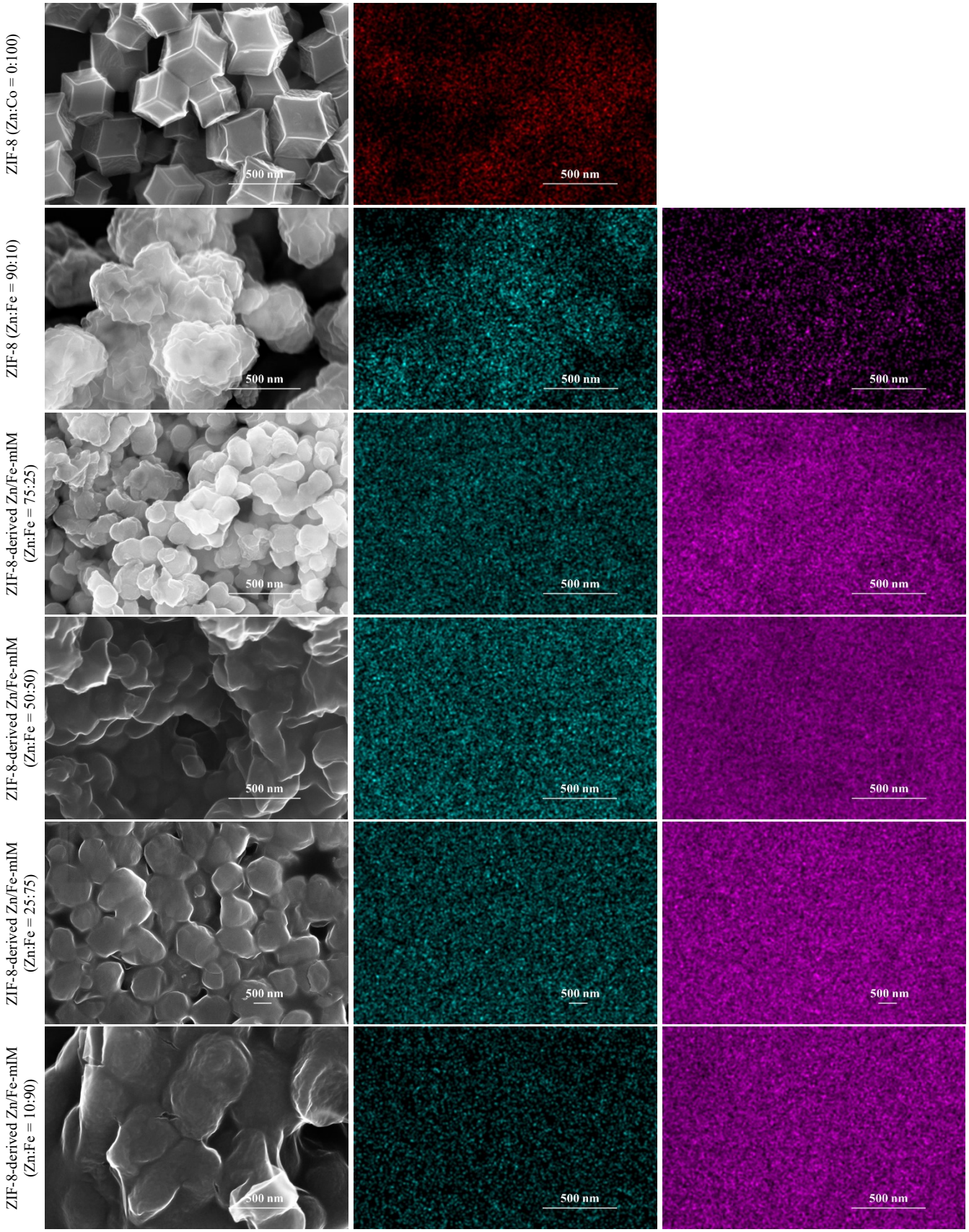
ZIF-8 (Zn:Co = 0:100)
ZIF-8 (Zn:Fe = 90:10)
ZIF-8-derived Zn/Fe-mIM (Zn:Fe = 75:25)
ZIF-8-derived Zn/Fe-mIM (Zn:Fe = 50:50)
ZIF-8-derived Zn/Fe-mIM (Zn:Fe = 25:75)
ZIF-8-derived Zn/Fe-mIM (Zn:Fe = 10:90)
500 nm

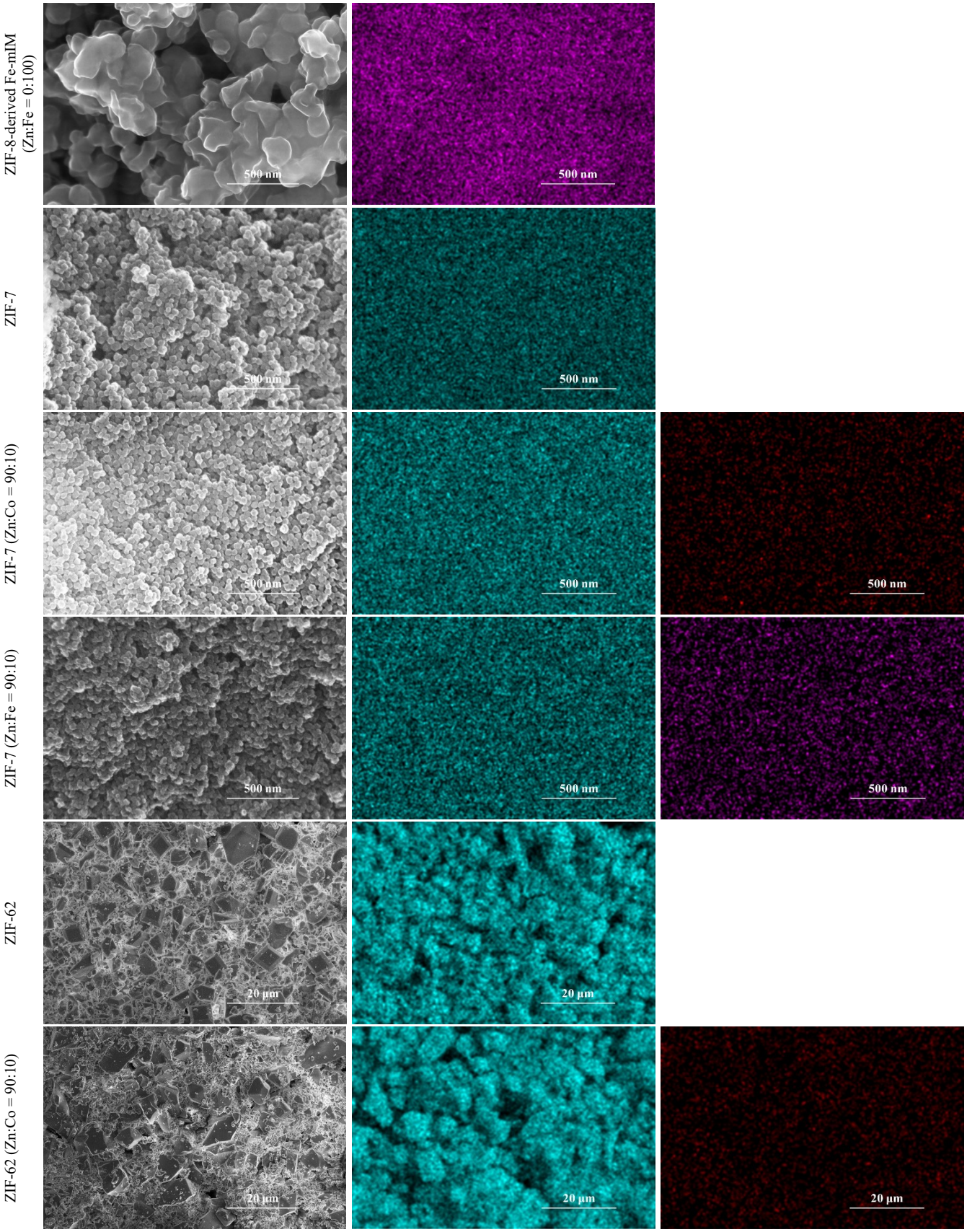
ZIF-8-derived Fe-mIM (Zn:Fe = 0:100)
ZIF-7
ZIF-7 (Zn:Co = 90:10)
ZIF-7 (Zn:Fe = 90:10)
ZIF-62
ZIF-62 (Zn:Co = 90:10)
500 nm
20 μm

ZIF-62 (Zn:Fe = 90:10)

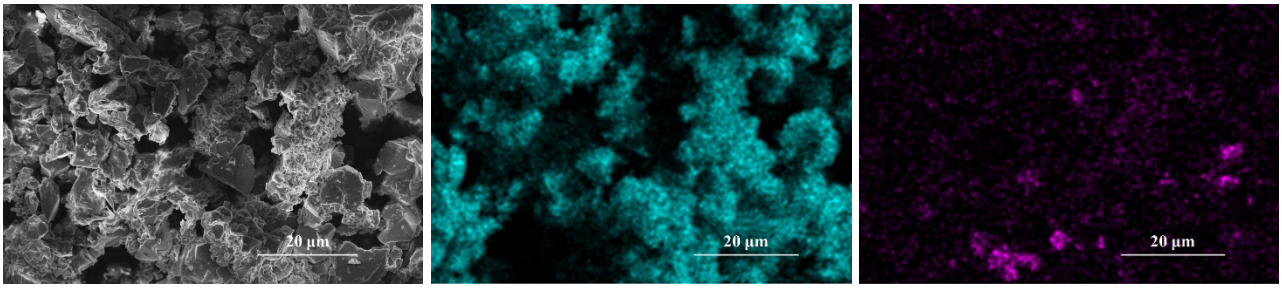

Figure S9. The SEM/EDX images of ZIF-8, its associated Co bimetallic structures, and the Zn/Fe-mIM series (ZIF-8 (Zn:Fe = 90:10) and ZIF-8-derived Zn/Fe-mIM materials for Zn:Fe = 75:25-0:100) as well as ZIF-7, and ZIF-62, and their respective bimetallic derivatives, synthesised using the MS method (in the images, cyan represents Zn, red represents Co, and magenta represents Fe).

Figure S10 provides the SEM/EDX images of ZIF-8, ZIF-62, and their bimetallic derivatives (Zn:Co = 90:10 and Zn:Fe = 90:10, respectively) synthesised using various methods including MS, OS, US, OS & US, BM, and MW. The findings underscore the influence of synthesis methods on the morphology, particle size, and elemental distribution of ZIFs.

The SEM analysis of ZIF-8 crystals synthesised using various methods demonstrates significant differences in morphology, particle size, and uniformity. The MS method yields crystals with a rhombic dodecahedral morphology and uniform size, indicating a controlled synthesis process. The OS method yields comparable rhombic dodecahedral crystals with consistent morphology; however, the particles are slightly larger than those observed with the MS method owing to variations in mixing dynamics. In contrast, the US method produces particles with less distinct morphologies (approximately spherical or slightly faceted) that exhibit uniform size but are slightly smaller than those synthesised by the MS method, perhaps owing to the rapid nucleation and growth induced by ultrasound. The OS & US method yields rhombic dodecahedral crystals similar to those produced by the OS method with uniform size that are larger than those synthesised by the US method, indicating a synergistic impact of both methods. The BM method produces particles that retain rhombic-dodecahedral faceting, but

they are commonly intergrown/aggregated with rounded edges and variable sizes. On the other hand, the MW method produces rod-like crystals characterised by irregular shapes, poor homogeneity, and rough surfaces, along with a larger size compared to all other methods, possibly attributable to the rapid heating and nucleation inherent in MW-assisted synthesis, leading to less controlled growth. EDX confirms the presence of Zn, demonstrating a consistent and uniform distribution of Zn in ZIF-8 crystals across the various synthesis methods.

ZIF-8 (Zn:Co = 90:10) exhibits similar results to ZIF-8 across several synthesis methods, with minor discrepancies seen in the US and MW methods. The US method results in particles that are slightly larger than those generated by the MS method. The increase in particle size may be ascribed to the effect of Co substitution on nucleation and growth kinetics under ultrasonic conditions. The MW method produces more homogeneous rod-like crystals, demonstrating a substantial influence of MW heating on crystal growth in the presence of Co. EDX also verifies the presence of both Zn and Co in the crystals, with Zn as the main element and Co as the minor one, consistently distributed across all synthesis methods.

As shown in SEM images, ZIF-62 synthesised using the MS method yields irregular, porous particles with significant aggregation, indicating poor control over synthesis. In contrast, the OS method results in more distinct polyhedral crystals with moderate aggregation. The US method produces uniformly sized, well-dispersed spherical particles owing to rapid nucleation. The OS & US method yields particles displaying both polyhedral and spherical shapes with improved homogeneity owing to synergistic effects. The BM method generates extremely irregular and fragmented particles which implies mechanical disruption. The MW method leads to agglomerated, irregular particles. Moreover, the uniform distribution of Zn across all methods is confirmed by EDX analysis, with the US and MW methods demonstrating the highest homogeneity.

The synthesis of ZIF-62 (Zn:Fe = 90:10) using the MS method results in particles that are heavily aggregated and amorphous, with more unclear boundaries. This suggests that Fe can be a factor in preventing crystal growth. The OS method results in smaller, irregular polyhedral crystals with higher aggregation, which suggests that Fe has an impact on the homogeneity and size of the crystals.

Compact, spherical particles are generated using the US method; however, PXRD shows increased peak broadening/reduced long-range order for the US method sample relative to the MS method (**Figure S2d**), consistent with smaller coherent scattering domains and/or increased defect/strain content. The OS & US method produces heterogeneous morphologies with reduced uniformity, which is in contrast to the synergistic enhancement observed in the Fe-free system. The BM method continues to produce irregular, fragmentary particles with minimal morphological variation, indicating that mechanical forces are more significant than compositional influences. The introduction of Fe results in fused, dense particles with less distinct edges, in contrast to the polyhedral crystals generated by the MW method of ZIF-62. The uniform distribution of Zn and Fe across all samples is verified by EDX, with Zn being the predominant element and Fe a minor one.

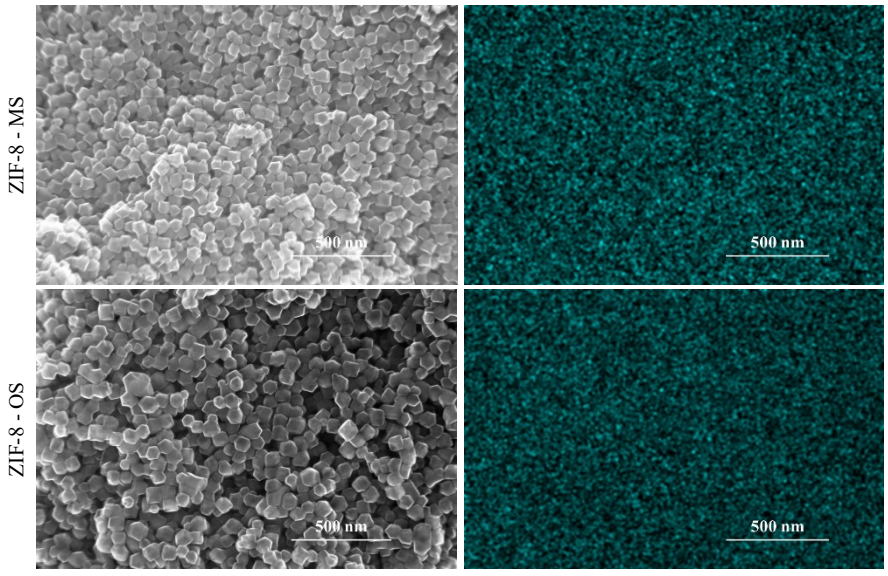

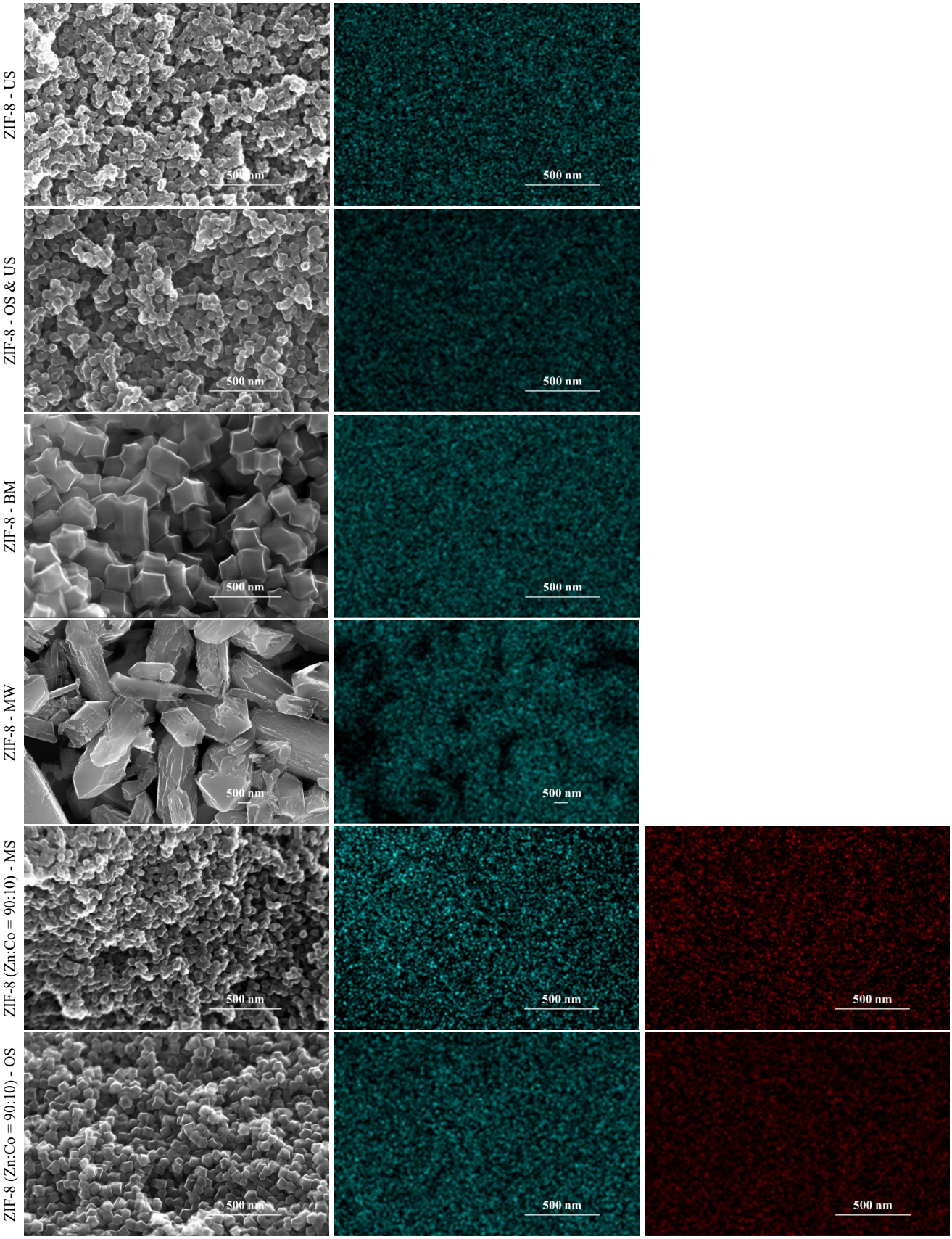
ZIF-8 - US
ZIF-8 - OS & US
ZIF-8 - BM
ZIF-8 - MW
ZIF-8 (Zn:Co = 90:10) - MS
ZIF-8 (Zn:Co = 90:10) - OS
500 nm

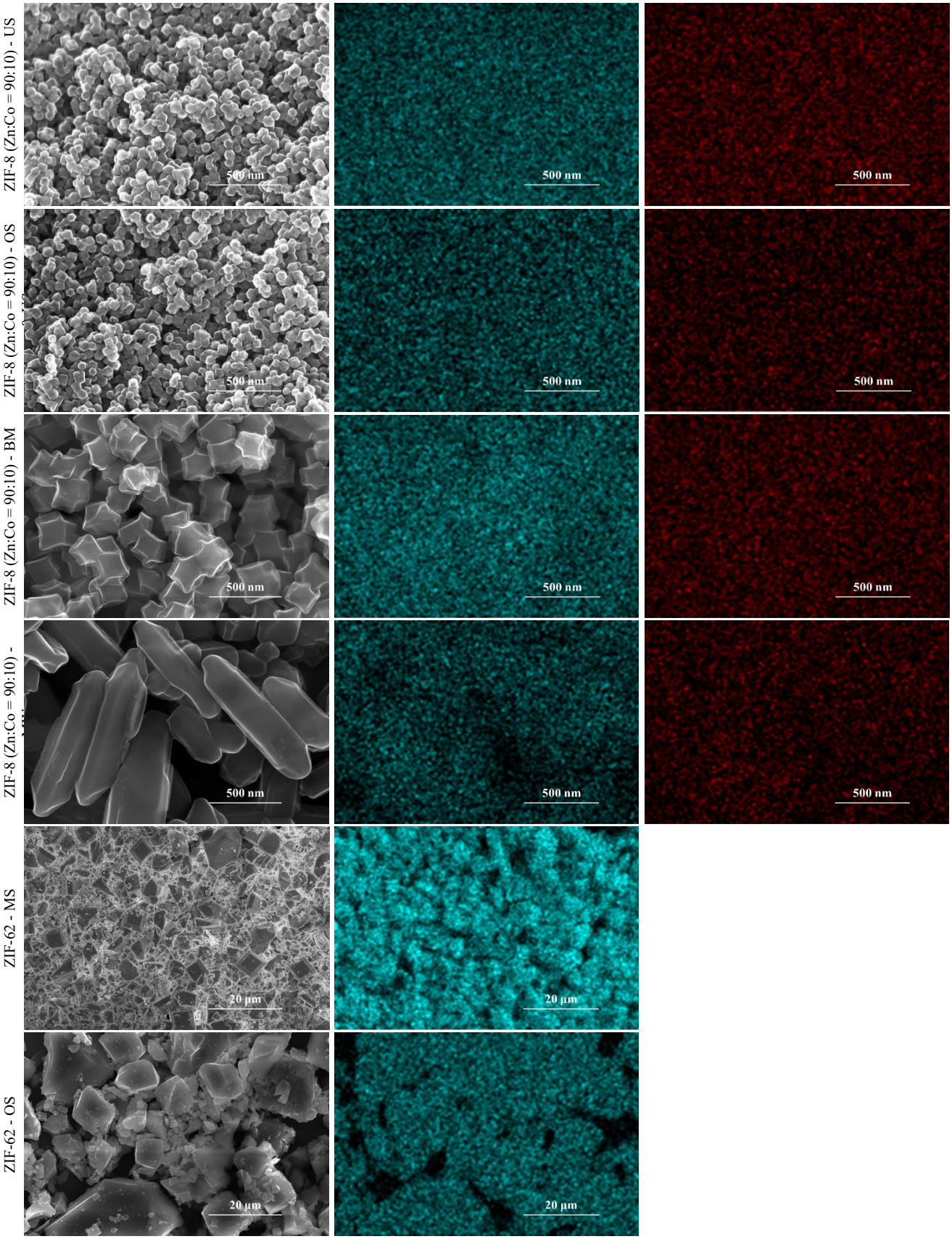
ZIF-8 (Zn:Co = 90:10) - US
ZIF-8 (Zn:Co = 90:10) - OS
ZIF-8 (Zn:Co = 90:10) - BM
ZIF-62 - MS
ZIF-62 - OS
500 nm
20 µm

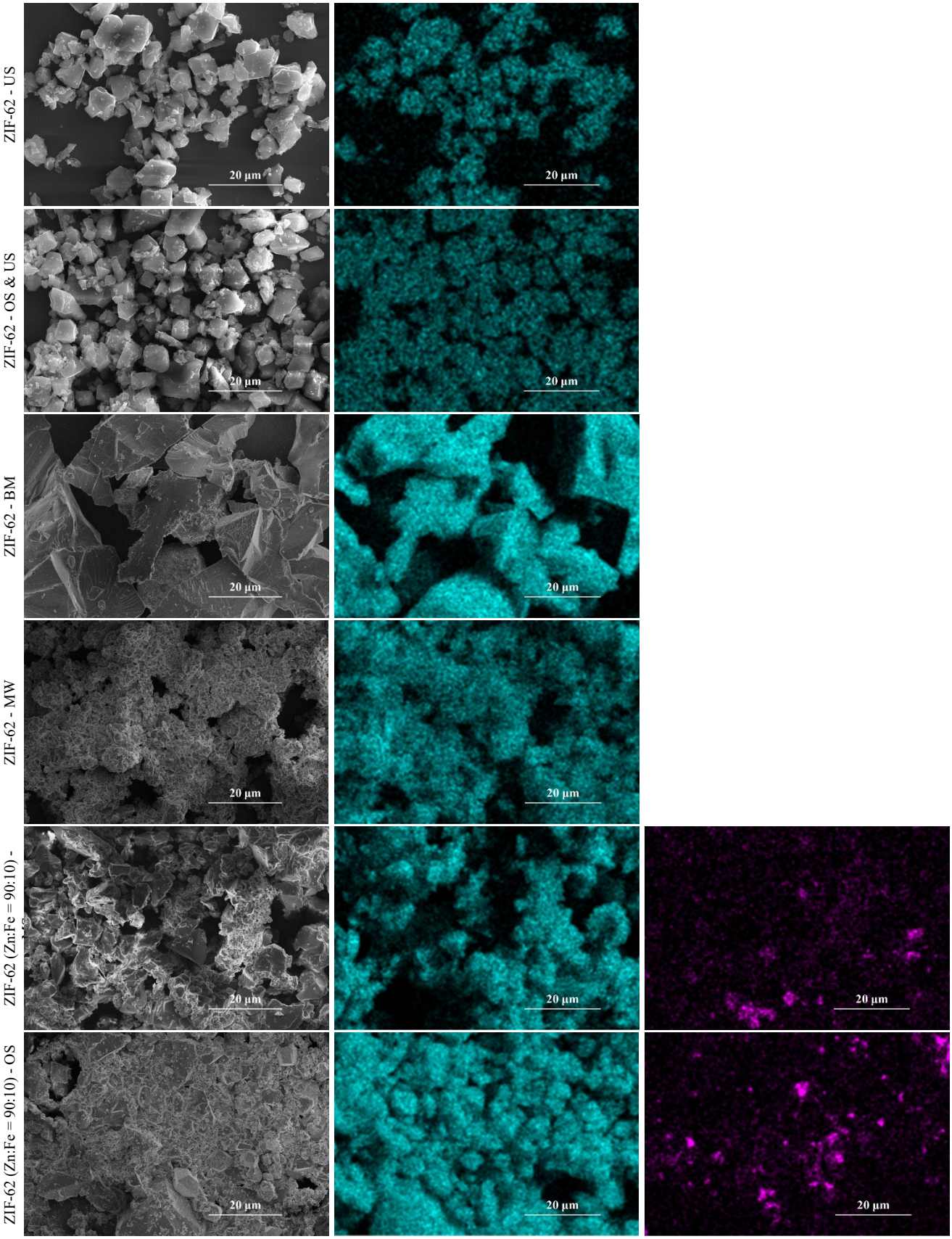
ZIF-62 - US
ZIF-62 - OS & US
ZIF-62 - BM
ZIF-62 - MW
ZIF-62 (Zn:Fe = 90:10) -
ZIF-62 (Zn:Fe = 90:10) - OS
20 µm

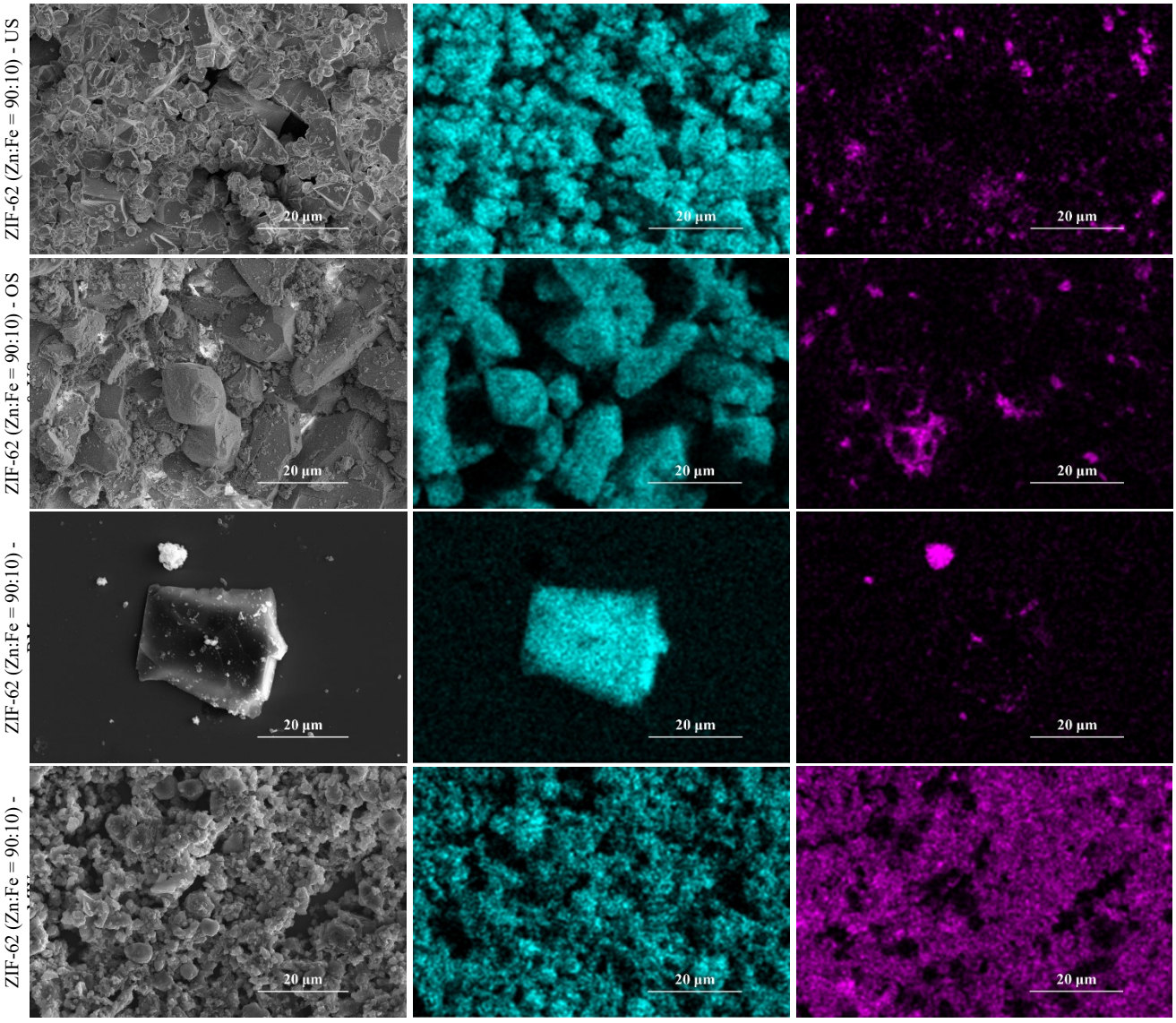

Figure S10. The SEM/EDX images of ZIF-8, ZIF-8 (Zn:Co = 90:10), ZIF-62, and ZIF-62 (Zn:Fe = 90:10), synthesised using the MS, OS, US, OS & US, BM, and MW methods (in the images, cyan represents Zn, red represents Co, and magenta represents Fe).

S8: Gas adsorption measurement

The oxygen (O_2) isotherms over multiple cycles and N_2 isotherms were determined using a Micromeritics 3Flex gas sorption analyser using ultra-high purity O_2 and N_2 gases. Before the measurement, the materials were activated in a vacuum at 160 °C for 24 h. O_2 and N_2 isotherms were obtained at 298 K throughout a pressure range of 0 to 1 bar, with the sample container maintained in a water bath for temperature stability.

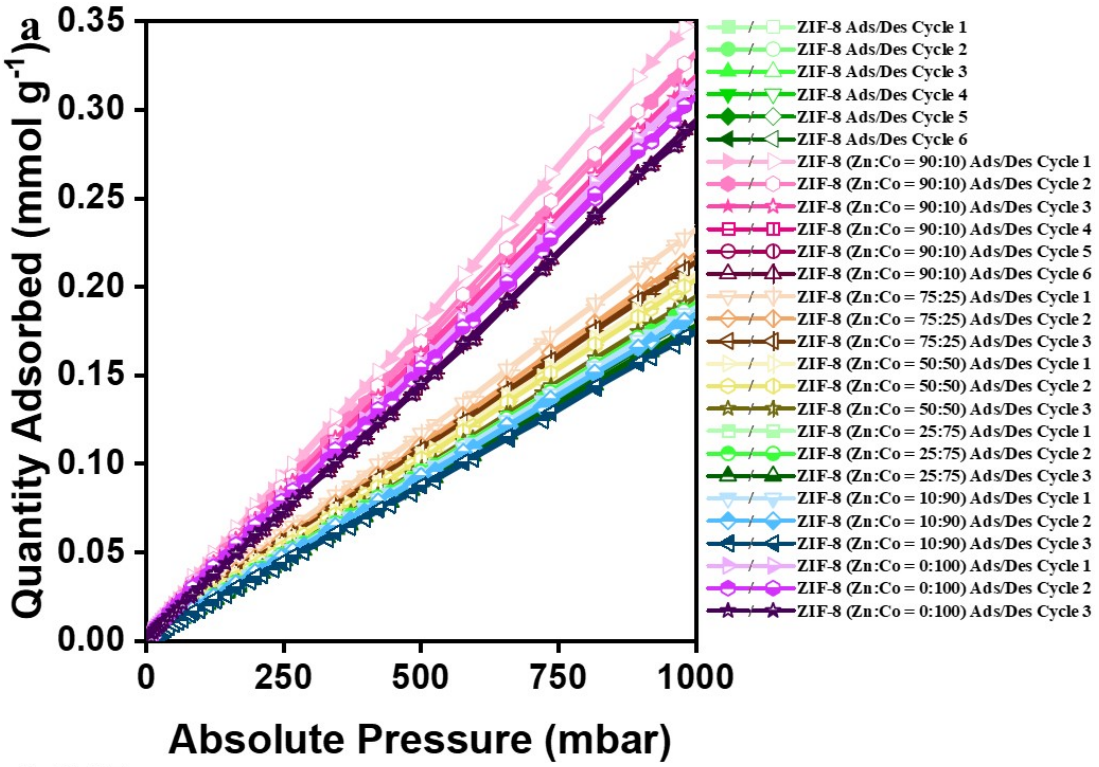
a
Quantity Adsorbed (mmol g-1)
0.00
0.05
0.10
0.15
0.20
0.25
0.30
0.35
0
250
500
750
1000
Absolute Pressure (mbar)
ZIF-8 Ads/Des Cycle 1
ZIF-8 Ads/Des Cycle 2
ZIF-8 Ads/Des Cycle 3
ZIF-8 Ads/Des Cycle 4
ZIF-8 Ads/Des Cycle 5
ZIF-8 Ads/Des Cycle 6
ZIF-8 (Zn:Co = 90:10) Ads/Des Cycle 1
ZIF-8 (Zn:Co = 90:10) Ads/Des Cycle 2
ZIF-8 (Zn:Co = 90:10) Ads/Des Cycle 3
ZIF-8 (Zn:Co = 90:10) Ads/Des Cycle 4
ZIF-8 (Zn:Co = 90:10) Ads/Des Cycle 5
ZIF-8 (Zn:Co = 90:10) Ads/Des Cycle 6
ZIF-8 (Zn:Co = 75:25) Ads/Des Cycle 1
ZIF-8 (Zn:Co = 75:25) Ads/Des Cycle 2
ZIF-8 (Zn:Co = 75:25) Ads/Des Cycle 3
ZIF-8 (Zn:Co = 50:50) Ads/Des Cycle 1
ZIF-8 (Zn:Co = 50:50) Ads/Des Cycle 2
ZIF-8 (Zn:Co = 50:50) Ads/Des Cycle 3
ZIF-8 (Zn:Co = 25:75) Ads/Des Cycle 1
ZIF-8 (Zn:Co = 25:75) Ads/Des Cycle 2
ZIF-8 (Zn:Co = 25:75) Ads/Des Cycle 3
ZIF-8 (Zn:Co = 10:90) Ads/Des Cycle 1
ZIF-8 (Zn:Co = 10:90) Ads/Des Cycle 2
ZIF-8 (Zn:Co = 10:90) Ads/Des Cycle 3
ZIF-8 (Zn:Co = 0:100) Ads/Des Cycle 1
ZIF-8 (Zn:Co = 0:100) Ads/Des Cycle 2
ZIF-8 (Zn:Co = 0:100) Ads/Des Cycle 3

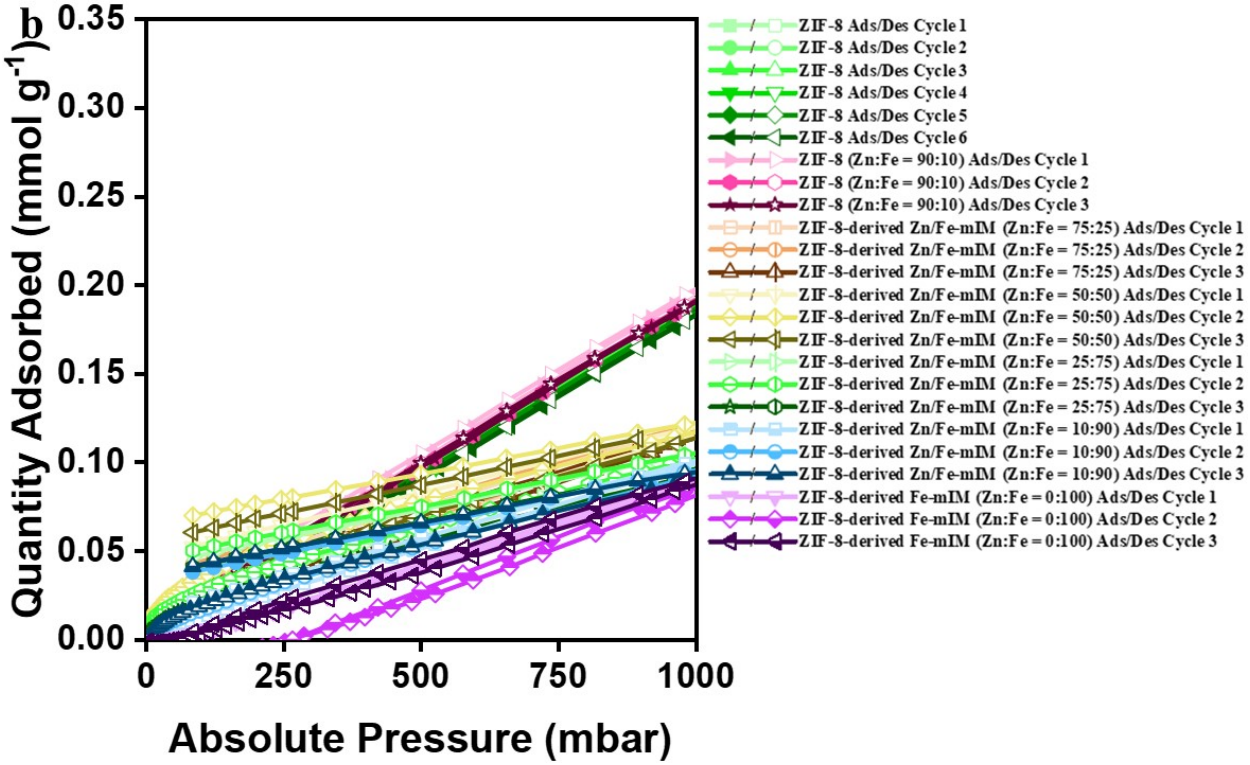
b
Quantity Adsorbed (mmol g-1)
0.00
0.05
0.10
0.15
0.20
0.25
0.30
0.35
0
250
500
750
1000
Absolute Pressure (mbar)
ZIF-8 Ads/Des Cycle 1
ZIF-8 Ads/Des Cycle 2
ZIF-8 Ads/Des Cycle 3
ZIF-8 Ads/Des Cycle 4
ZIF-8 Ads/Des Cycle 5
ZIF-8 Ads/Des Cycle 6
ZIF-8 (Zn:Fe = 90:10) Ads/Des Cycle 1
ZIF-8 (Zn:Fe = 90:10) Ads/Des Cycle 2
ZIF-8 (Zn:Fe = 90:10) Ads/Des Cycle 3
ZIF-8-derived Zn/Fe-mIM (Zn:Fe = 75:25) Ads/Des Cycle 1
ZIF-8-derived Zn/Fe-mIM (Zn:Fe = 75:25) Ads/Des Cycle 2
ZIF-8-derived Zn/Fe-mIM (Zn:Fe = 75:25) Ads/Des Cycle 3
ZIF-8-derived Zn/Fe-mIM (Zn:Fe = 50:50) Ads/Des Cycle 1
ZIF-8-derived Zn/Fe-mIM (Zn:Fe = 50:50) Ads/Des Cycle 2
ZIF-8-derived Zn/Fe-mIM (Zn:Fe = 50:50) Ads/Des Cycle 3
ZIF-8-derived Zn/Fe-mIM (Zn:Fe = 25:75) Ads/Des Cycle 1
ZIF-8-derived Zn/Fe-mIM (Zn:Fe = 25:75) Ads/Des Cycle 2
ZIF-8-derived Zn/Fe-mIM (Zn:Fe = 25:75) Ads/Des Cycle 3
ZIF-8-derived Zn/Fe-mIM (Zn:Fe = 10:90) Ads/Des Cycle 1
ZIF-8-derived Zn/Fe-mIM (Zn:Fe = 10:90) Ads/Des Cycle 2
ZIF-8-derived Zn/Fe-mIM (Zn:Fe = 10:90) Ads/Des Cycle 3
ZIF-8-derived Fe-mIM (Zn:Fe = 0:100) Ads/Des Cycle 1
ZIF-8-derived Fe-mIM (Zn:Fe = 0:100) Ads/Des Cycle 2
ZIF-8-derived Fe-mIM (Zn:Fe = 0:100) Ads/Des Cycle 3

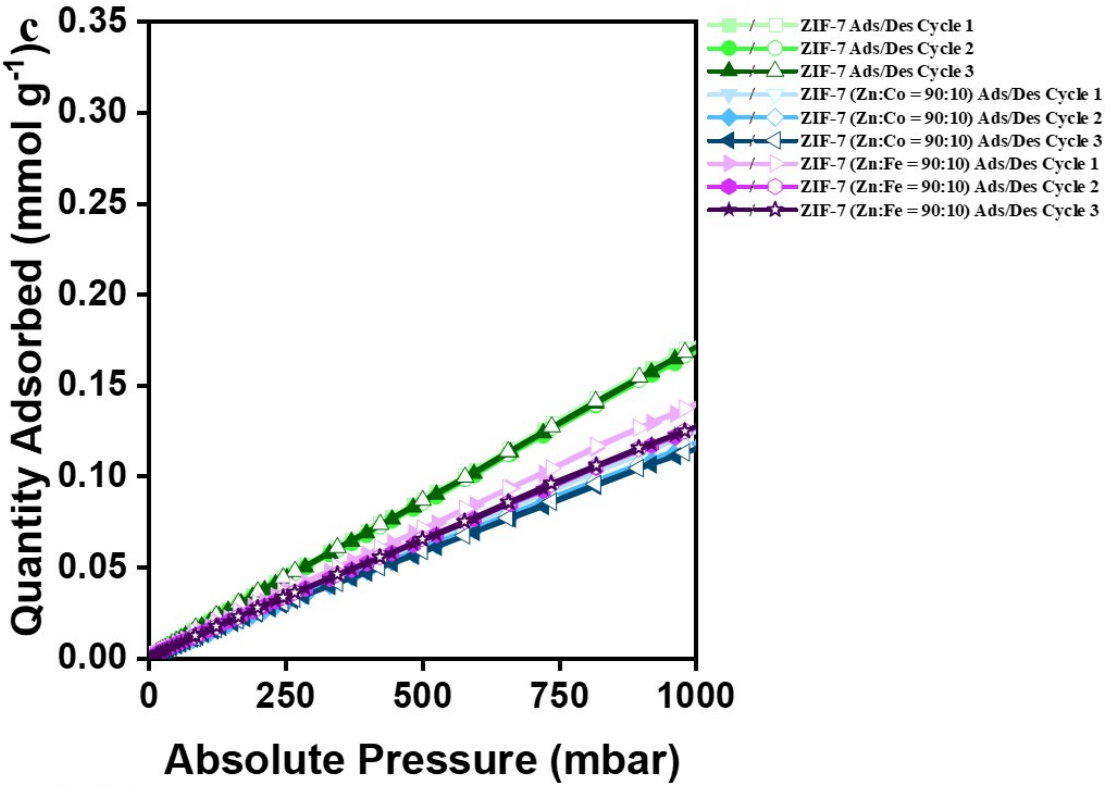

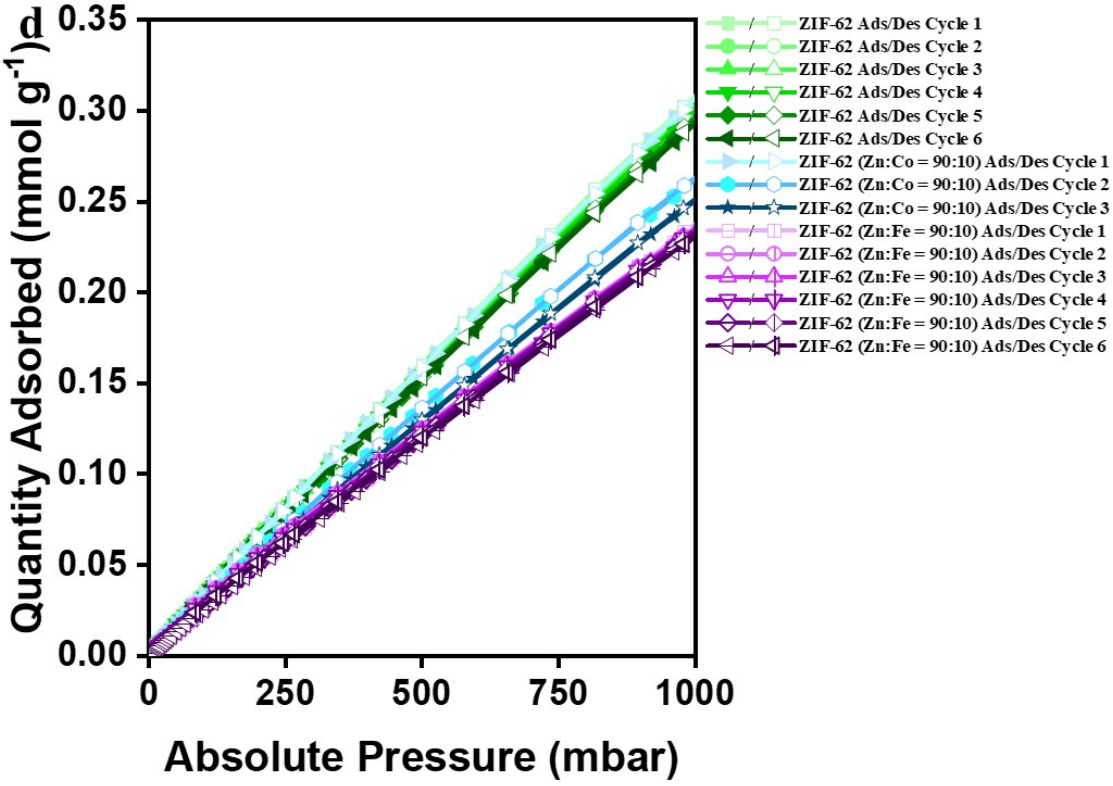

Figure S11. The O_2 isotherms over various cycles of a) ZIF-8 and its associated Co bimetallic structures, b) ZIF-8 and the Zn/Fe-mIM series (ZIF-8 (Zn:Fe = 90:10) and ZIF-8-derived Zn/Fe-mIM materials for Zn:Fe = 75:25-0:100), c) ZIF-7 and its associated Co and Fe

bimetallic structures, and d) ZIF-62 and its associated Co and Fe bimetallic structures, synthesised using the MS method and analysed with a 3Flex gas sorption analyser.

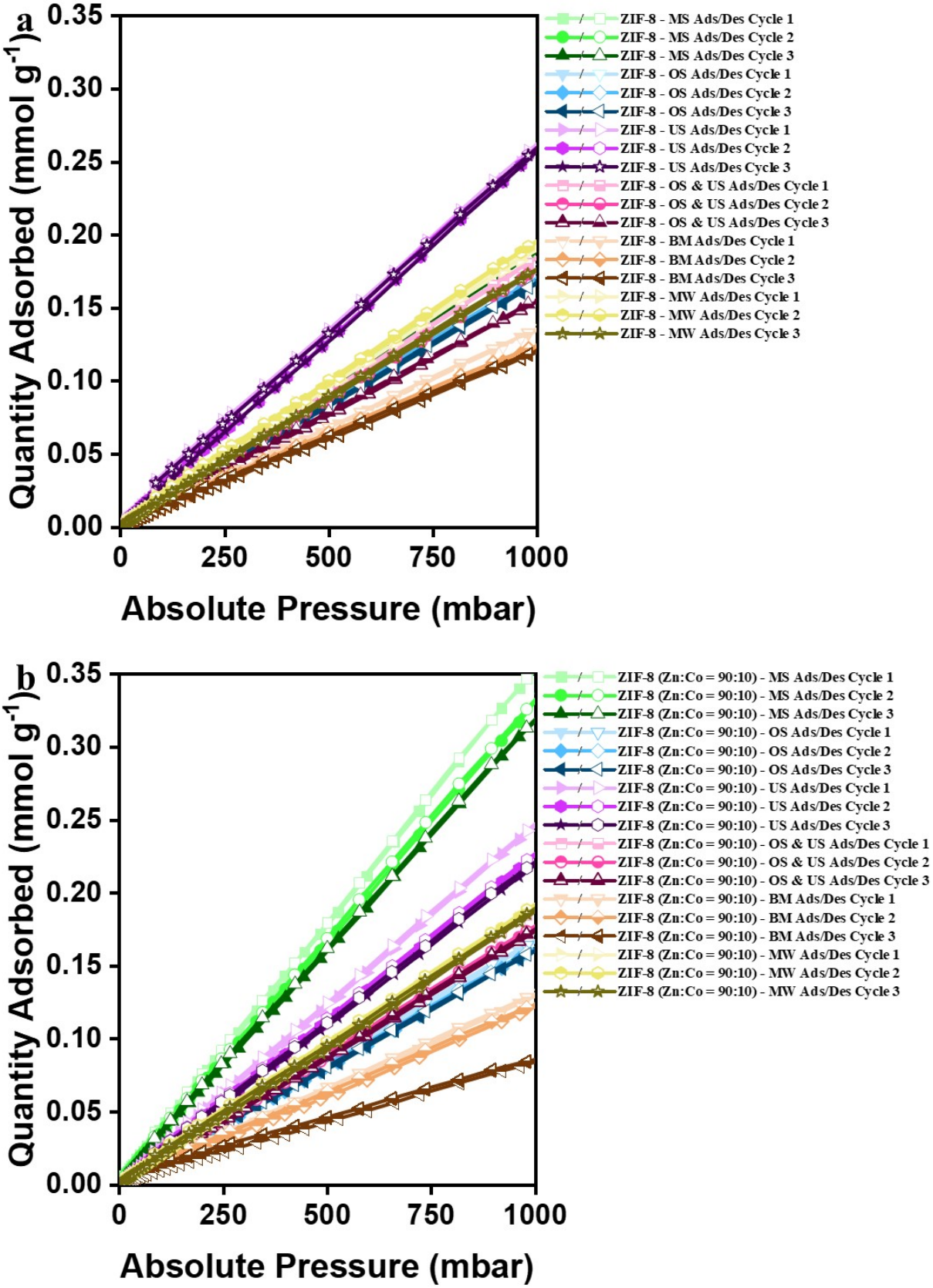

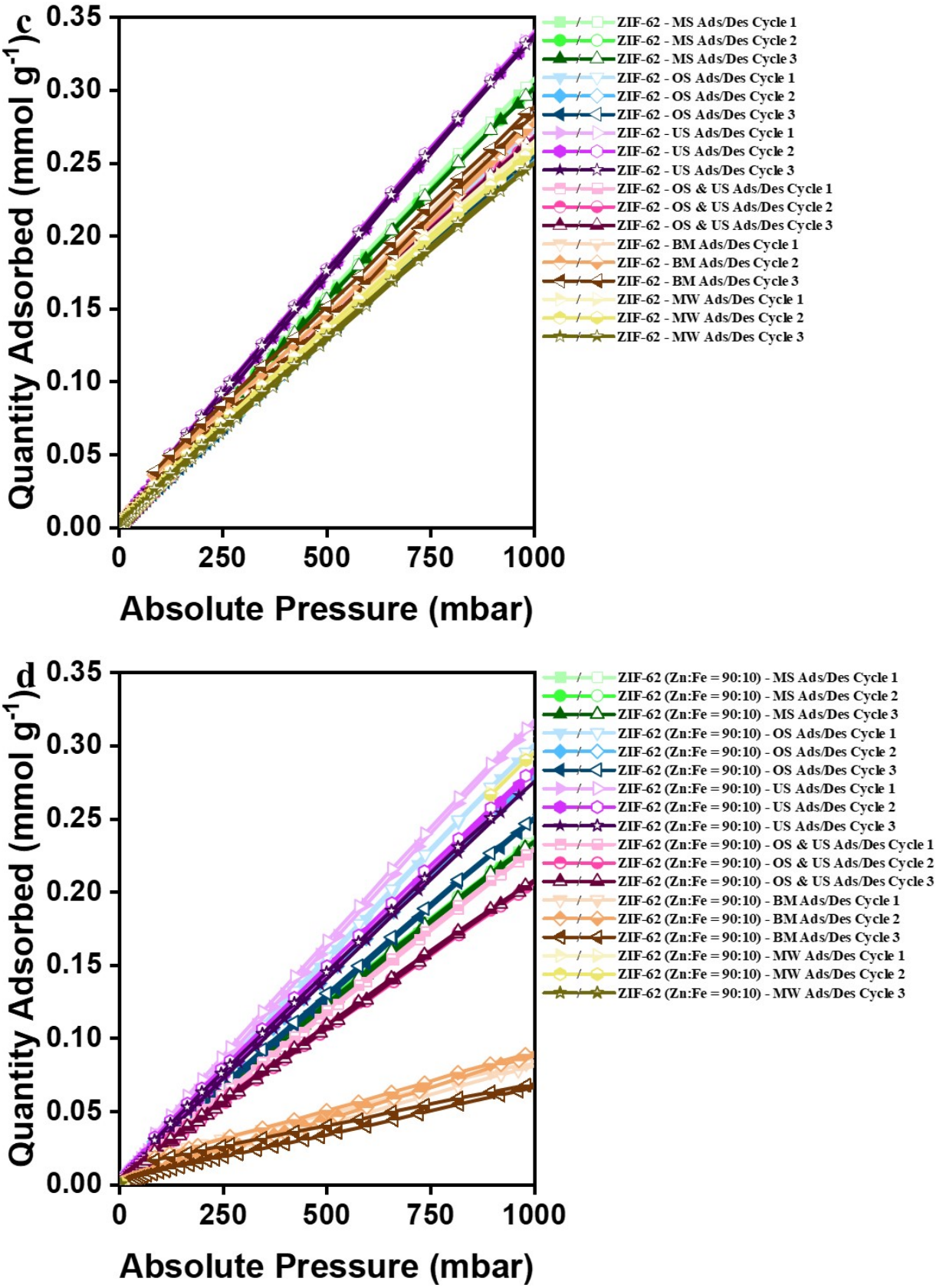

Figure S12. The O_2 isotherms over various cycles of a) ZIF-8, b) ZIF-8 (Zn:Co = 90:10), c)

ZIF-62, and d) ZIF-62 (Zn:Fe = 90:10), synthesised using the MS, OS, US, OS & US, BM, and MW methods, and analysed with a 3Flex gas sorption analyser.

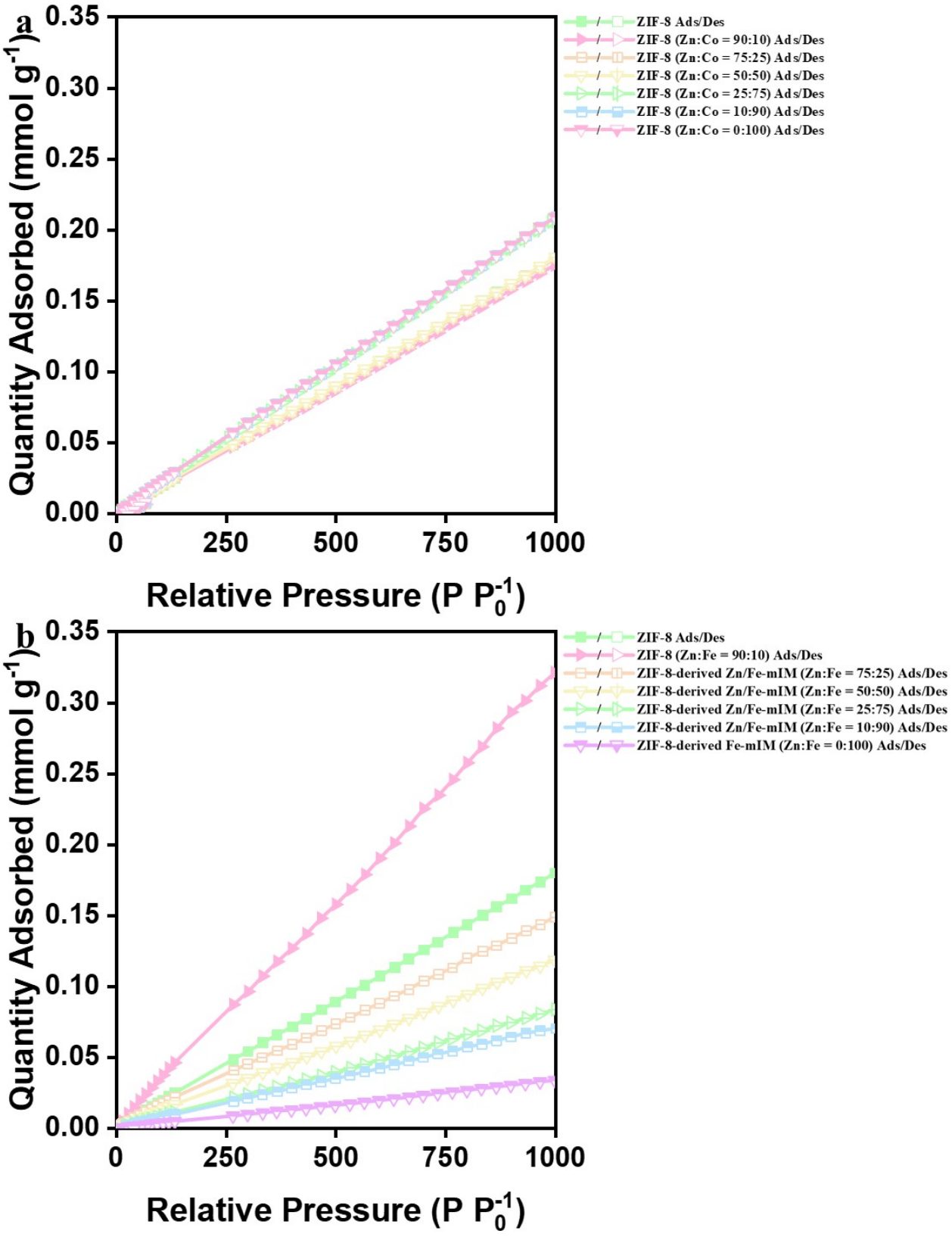

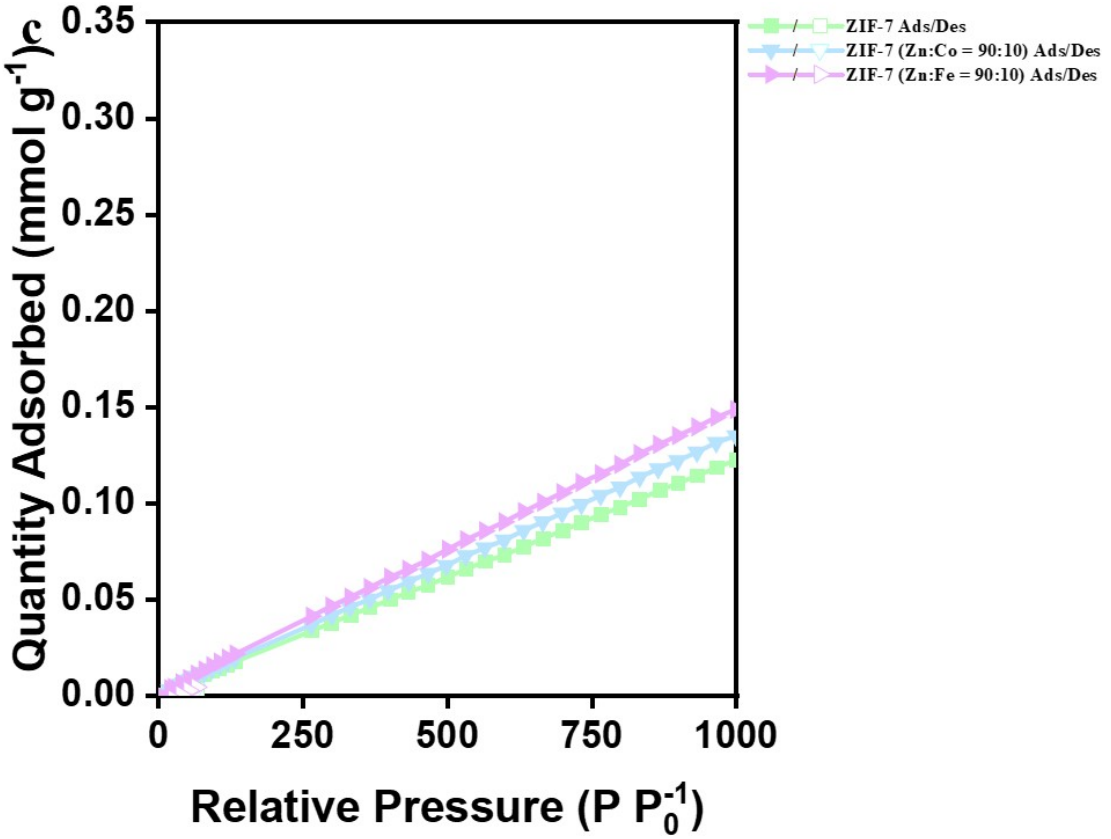
c
Quantity Adsorbed (mmol g-1)
0.35
0.30
0.25
0.20
0.15
0.10
0.05
0.00
0
250
500
750
1000
Relative Pressure (P P0-1)
ZIF-7 Ads/Des
ZIF-7 (Zn:Co = 90:10) Ads/Des
ZIF-7 (Zn:Fe = 90:10) Ads/Des

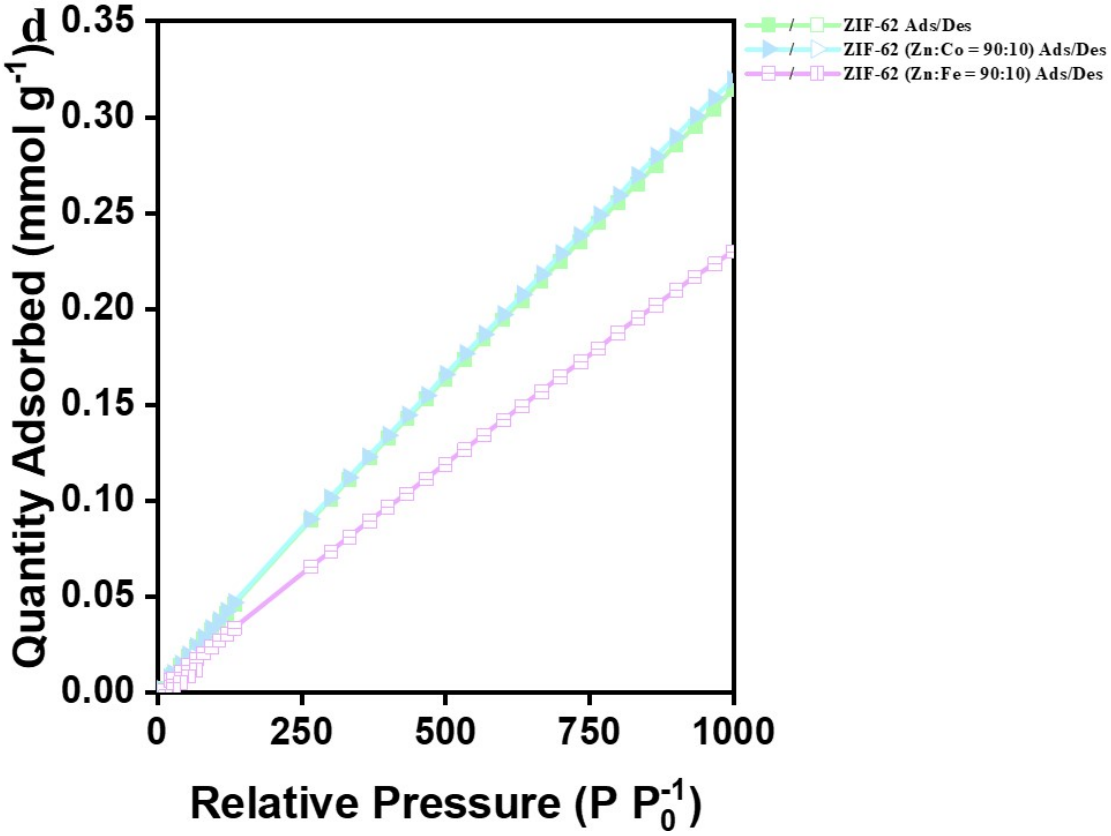
d
Quantity Adsorbed (mmol g-1)
0.35
0.30
0.25
0.20
0.15
0.10
0.05
0.00
0
250
500
750
1000
Relative Pressure (P P0-1)
ZIF-62 Ads/Des
ZIF-62 (Zn:Co = 90:10) Ads/Des
ZIF-62 (Zn:Fe = 90:10) Ads/Des

Figure S13. The N_2 isotherms of a) ZIF-8 and its associated Co bimetallic structures, b) ZIF-8 and the Zn/Fe-mIM series (ZIF-8 (Zn:Fe = 90:10) and ZIF-8-derived Zn/Fe-mIM materials for Zn:Fe = 75:25-0:100), c) ZIF-7 and its associated Co and Fe bimetallic structures, and d) ZIF-62 and its associated Co and Fe bimetallic structures, synthesised using the MS method and analysed with a 3Flex gas sorption analyser.

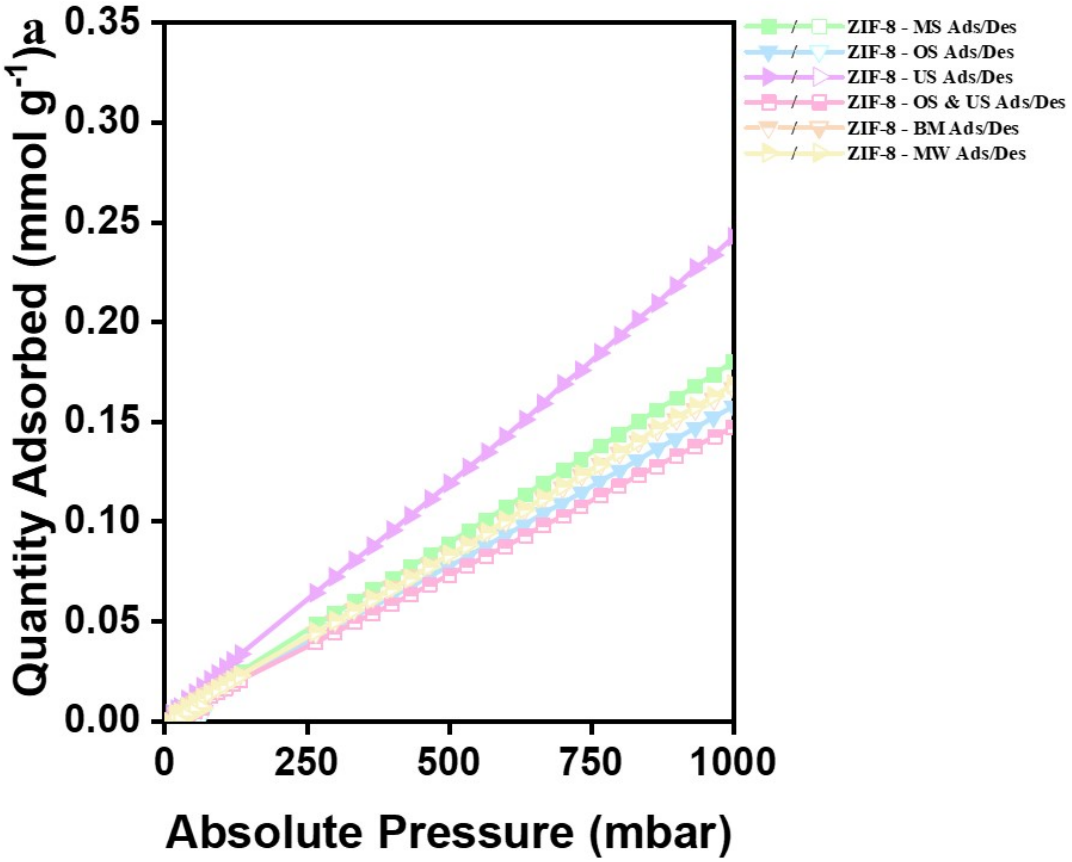

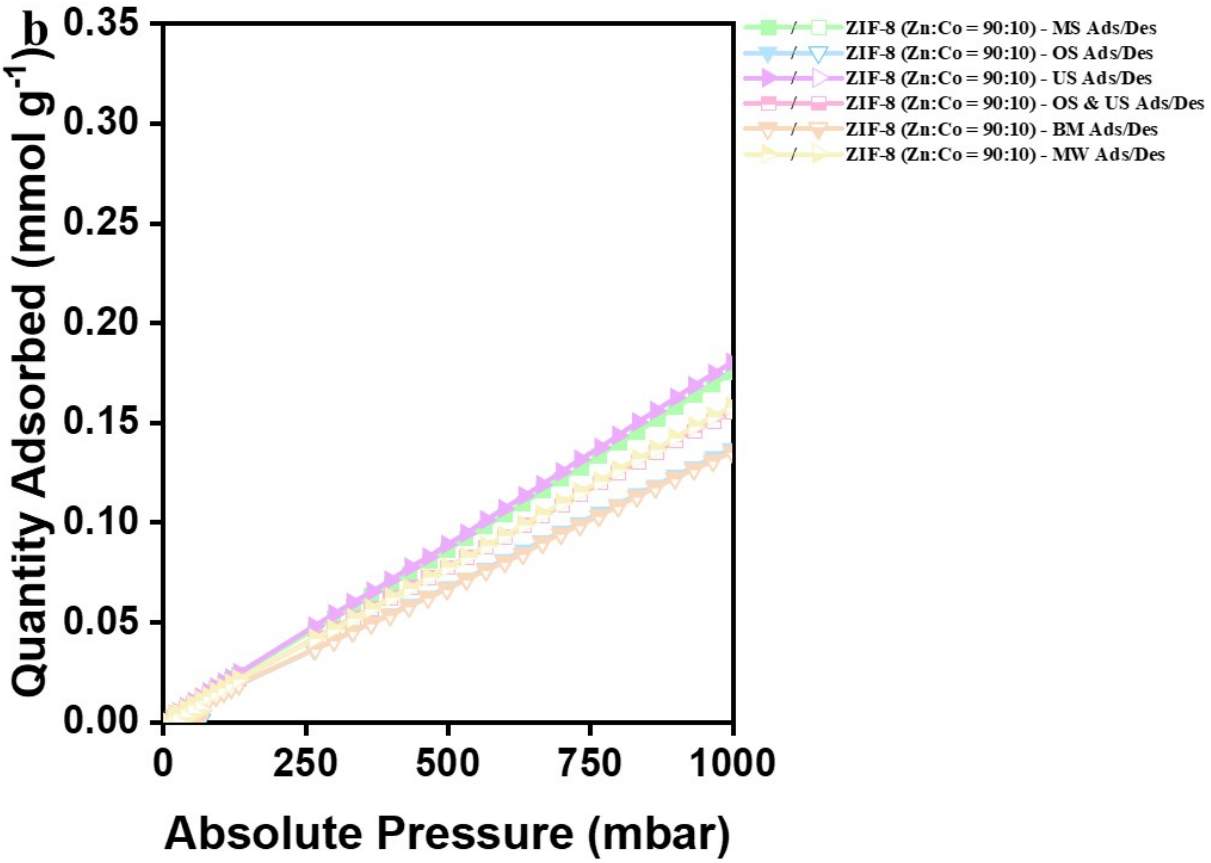
b
Quantity Adsorbed (mmol g-1)
0.35
0.30
0.25
0.20
0.15
0.10
0.05
0.00
0
250
500
750
1000
Absolute Pressure (mbar)
ZIF-8 (Zn:Co = 90:10) - MS Ads/Des
ZIF-8 (Zn:Co = 90:10) - OS Ads/Des
ZIF-8 (Zn:Co = 90:10) - US Ads/Des
ZIF-8 (Zn:Co = 90:10) - OS & US Ads/Des
ZIF-8 (Zn:Co = 90:10) - BM Ads/Des
ZIF-8 (Zn:Co = 90:10) - MW Ads/Des

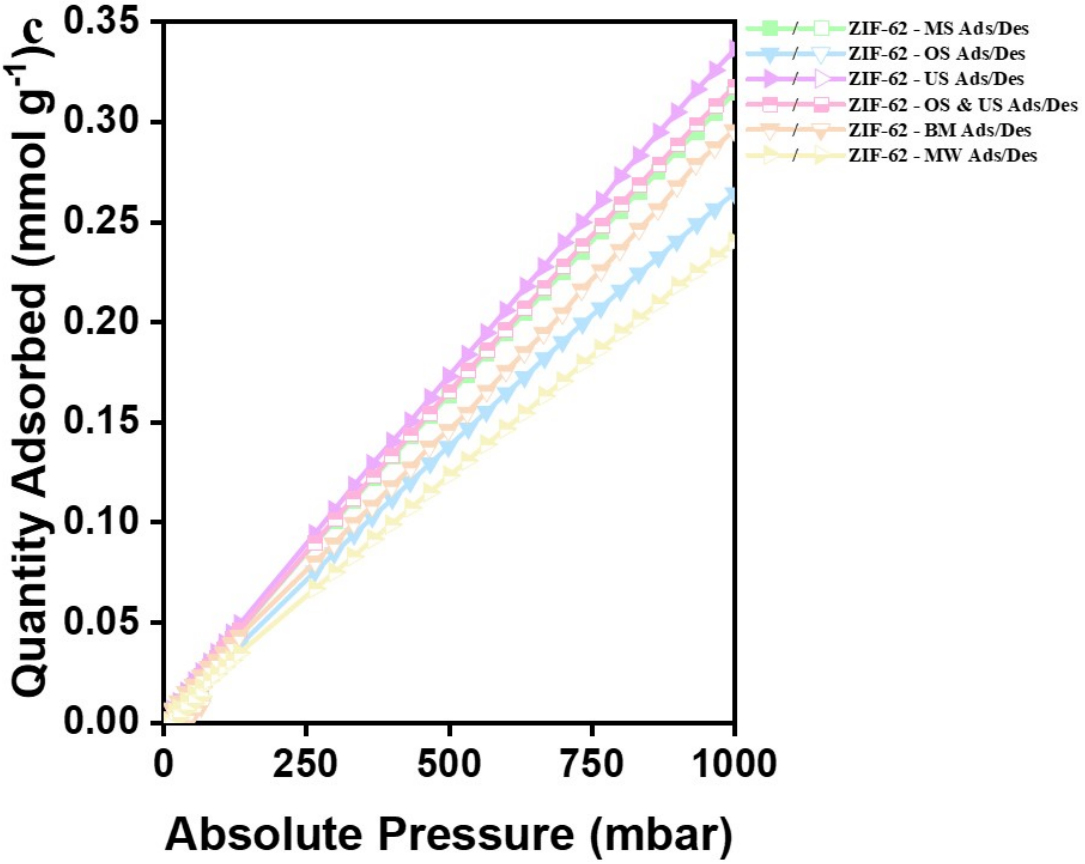
c
Quantity Adsorbed (mmol g-1)
0.35
0.30
0.25
0.20
0.15
0.10
0.05
0.00
0
250
500
750
1000
Absolute Pressure (mbar)
ZIF-62 - MS Ads/Des
ZIF-62 - OS Ads/Des
ZIF-62 - US Ads/Des
ZIF-62 - OS & US Ads/Des
ZIF-62 - BM Ads/Des
ZIF-62 - MW Ads/Des

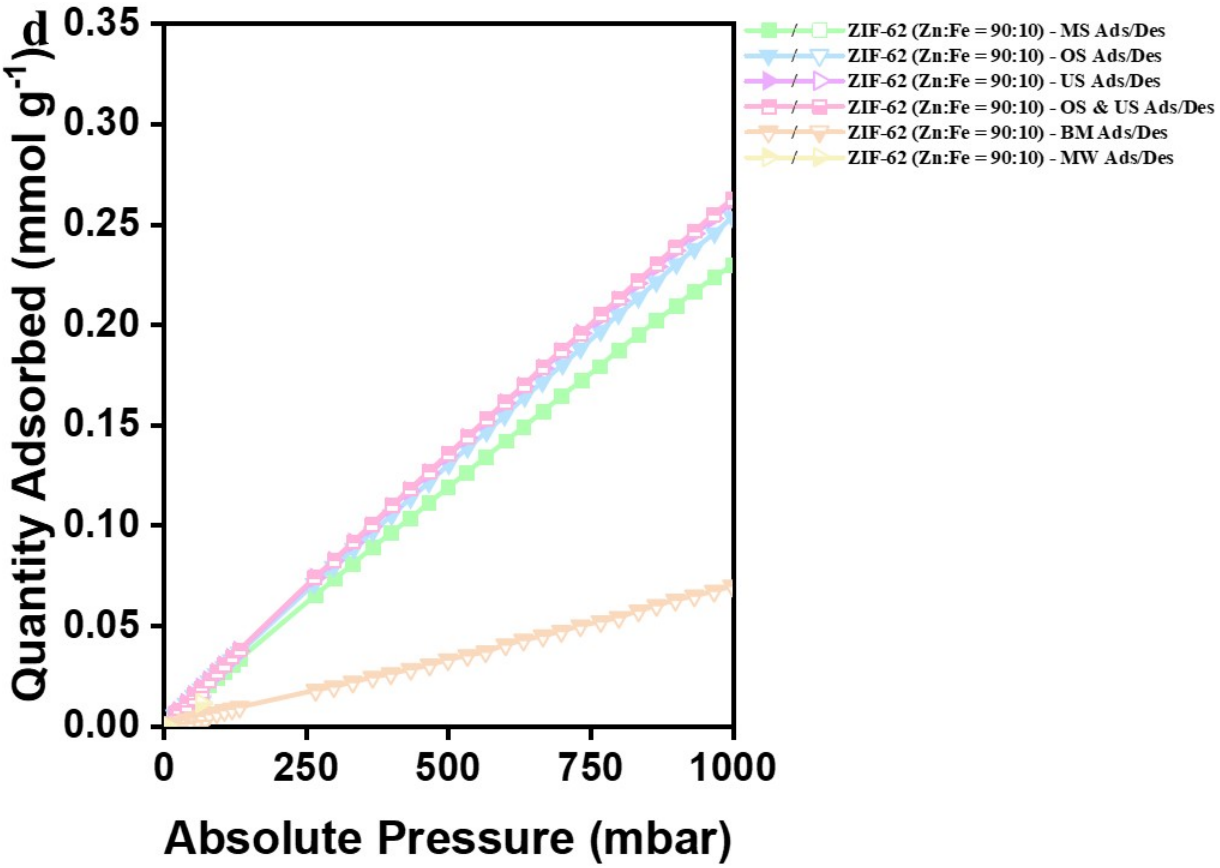

Figure S14. The N_2 isotherms over various cycles of a) ZIF-8, b) ZIF-8 (Zn:Co = 90:10), c) ZIF-62, and d) ZIF-62 (Zn:Fe = 90:10), synthesised using the MS, OS, US, OS & US, BM, and MW methods, and analysed with a 3Flex gas sorption analyser.

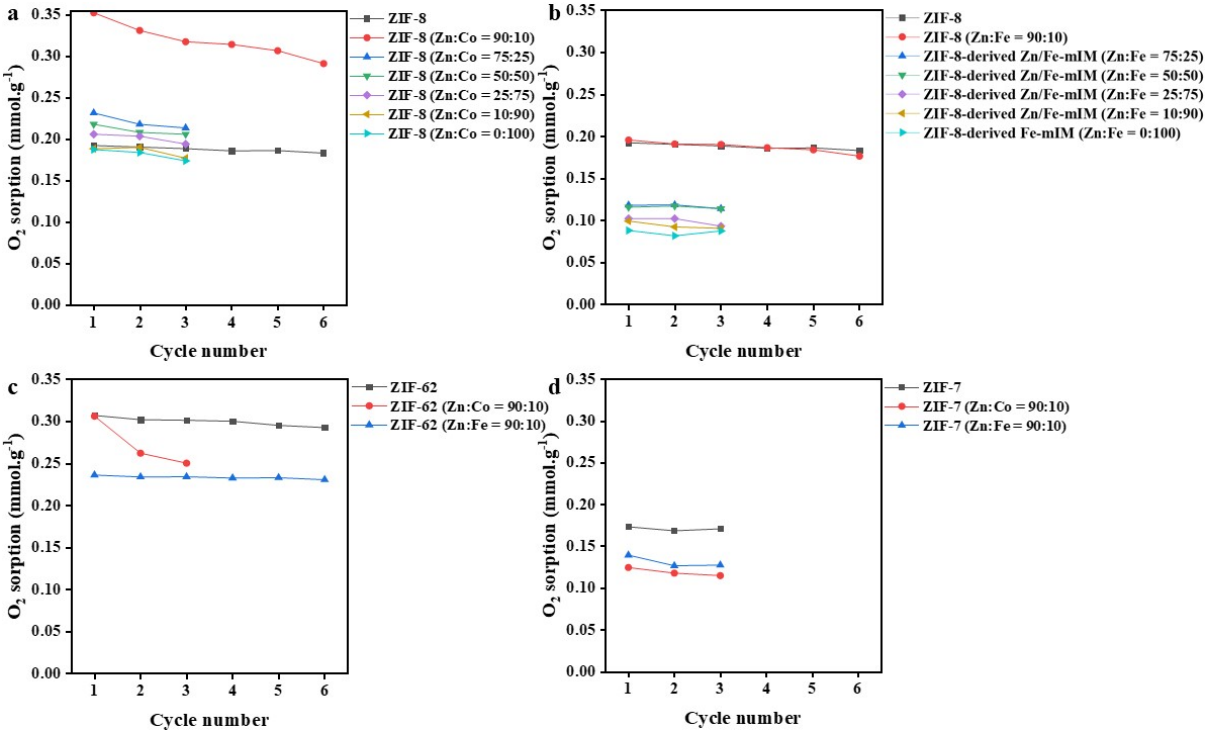

Figure S15. The O_2 sorption as a function of cycles for a) ZIF-8 and its associated Co bimetallic structures, b) ZIF-8 and the Zn/Fe-mIM series (ZIF-8 (Zn:Fe = 90:10) and ZIF-8-derived Zn/Fe-mIM materials for Zn:Fe = 75:25-0:100), c) ZIF-7 and its associated Co and Fe bimetallic structures, and d) ZIF-62 and its associated Co and Fe bimetallic structures, synthesised using the MS method and analysed with a 3Flex gas sorption analyser.

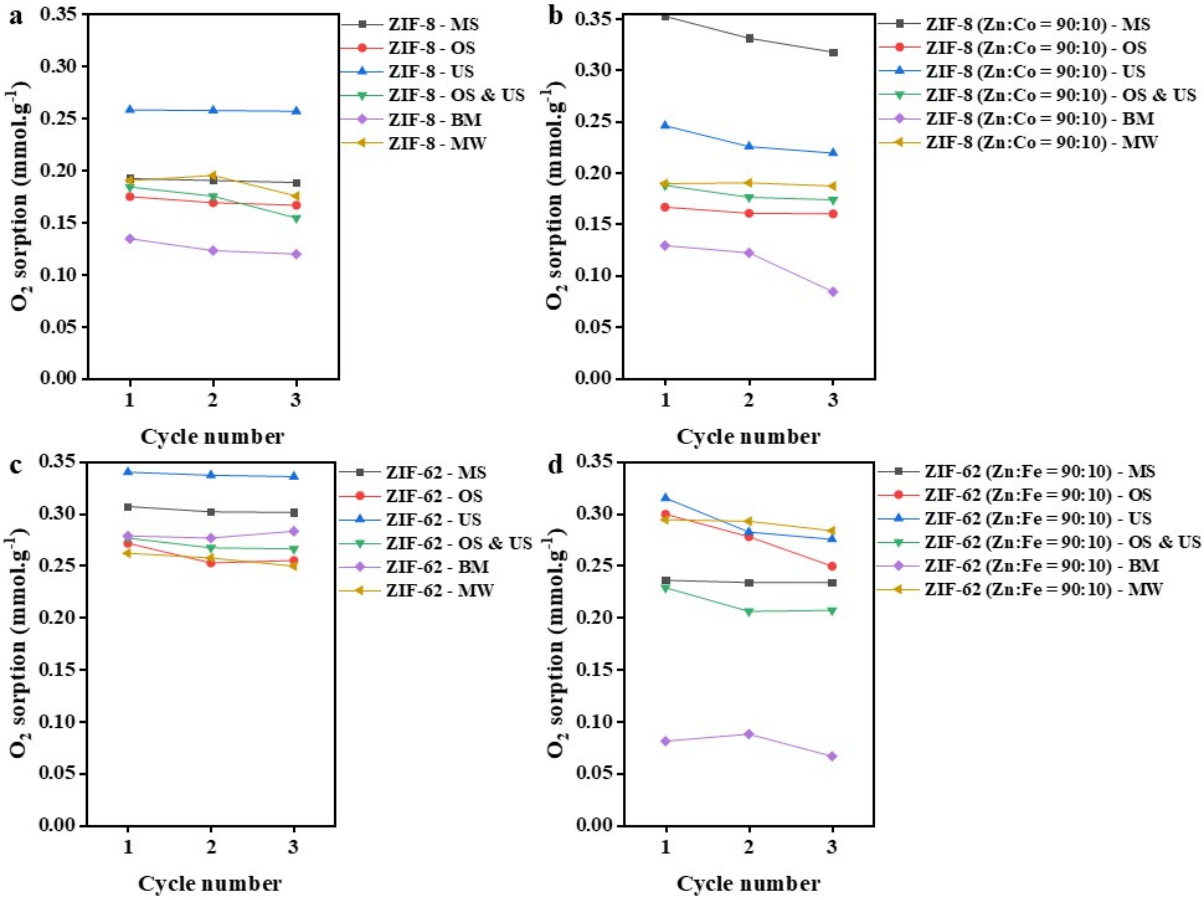

Figure S16. The O_2 sorption as a function of cycles for a) ZIF-8, b) ZIF-8 (Zn:Co = 90:10), c) ZIF-62, and d) ZIF-62 (Zn:Fe = 90:10), synthesised using the MS, OS, US, OS & US, BM, and MW methods, and analysed with a 3Flex gas sorption analyser.

S9: O_2/N_2 selectivity

The O_2/ N_2 selectivity was assessed via O_2 and N_2 isotherms measured on a 3Flex gas sorption analyser under identical conditions. The selectivity values were calculated from the ratio of O_2 to N_2 sorption at 1 bar and 298 K. The measurements were conducted after activating the material in a vacuum at 160 °C for 24 h to ensure the removal of adsorbed gases. The selectivity values shown in **Table S3** provide insights into the affinity of each material for O_2 over N_2, highlighting their potential in gas separation applications. **Table S4** further explores the effects of various synthesis methods (MS, OS, US, OS & US, BM, MW) on the O_2/N_2 selectivity.

Table S3. The O_2/N_2 selectivity of ZIF-7, ZIF-8, ZIF-62, and their respective bimetallic derivatives at 1 bar and 298 K, synthesised using the MS method.

Sample	O_2/N_2 selectivity
ZIF-7	1.42
ZIF-7 (Zn:Co = 90:10)	0.92
ZIF-7 (Zn:Fe = 90:10)	0.94
ZIF-62	0.98
ZIF-62 (Zn:Co = 90:10)	0.96
ZIF-62 (Zn:Fe = 90:10)	1.03
ZIF-8	1.07
ZIF-8 (Zn:Co = 90:10)	2.01
ZIF-8 (Zn:Co = 75:25)	1.29
ZIF-8 (Zn:Co = 50:50)	1.21
ZIF-8 (Zn:Co = 25:75)	1.14
ZIF-8 (Zn:Co = 10:90)	0.89
ZIF-8 (Zn:Co = 0:100)	0.90
ZIF-8 (Zn:Fe = 90:10)	0.61
ZIF-8-derived Zn/Fe-mIM (Zn:Fe = 75:25)	0.79
ZIF-8-derived Zn/Fe-mIM (Zn:Fe = 50:50)	0.98
ZIF-8-derived Zn/Fe-mIM (Zn:Fe = 25:75)	1.22
ZIF-8-derived Zn/Fe-mIM (Zn:Fe = 10:90)	1.41
ZIF-8-derived Fe-mIM (Zn:Fe = 0:100)	2.60

Table S4. The O_2/N_2 selectivity of ZIF-8, ZIF-8 (Zn:Co = 90:10), ZIF-62, and ZIF-62 (Zn:Fe = 90:10), synthesised using the MS, OS, US, OS & US, BM, and MW methods at 1 bar and 298 K.

MOF	O_2/N_2 selectivity
ZIF-8 - MS	1.07
ZIF-8 - OS	1.03
ZIF-8 - US	1.06
ZIF-8 - OS & US	1.25
ZIF-8 - BM	0.81
ZIF-8 - MW	1.13
ZIF-8 (Zn:Co = 90:10) - MS	2.01
ZIF-8 (Zn:Co = 90:10) - OS	1.22
ZIF-8 (Zn:Co = 90:10) - US	1.37
ZIF-8 (Zn:Co = 90:10) - OS & US	1.21
ZIF-8 (Zn:Co = 90:10) - BM	0.95
ZIF-8 (Zn:Co = 90:10) - MW	1.20
ZIF-62 - MS	0.98
ZIF-62 - OS	1.03
ZIF-62 - US	1.01
ZIF-62 - OS & US	0.87
ZIF-62 - BM	0.94

ZIF-62 - MW	1.09
ZIF-62 (Zn:Fe = 90:10) - MS	1.03
ZIF-62 (Zn:Fe = 90:10) - OS	1.18
ZIF-62 (Zn:Fe = 90:10) - US	1.20
ZIF-62 (Zn:Fe = 90:10) - OS & US	0.87
ZIF-62 (Zn:Fe = 90:10) - BM	1.16
ZIF-62 (Zn:Fe = 90:10) - MW	1.15

S9: O_2/N_2 selectivity

Table S5 presents a representative comparison of O_2 adsorption and O_2/N_2 selectivity for porous adsorbents that are closely related to the present study (e.g., ZIF-based materials and commonly used benchmark adsorbents such as zeolites). Due to the variation in experimental protocols for literature data, the measurement conditions (temperature, gas composition, and pressure) and the definition of selectivity employed in each reference (e.g., adsorption ratio at a specified pressure, Henry's constant ratio, or values obtained from isotherm fits) are explicitly specified to facilitate transparent benchmarking. Moreover, recyclability is also summarised by the documented variation in O_2 adsorption throughout multiple cycles when applicable.

Table S5. Literature comparison of O_2 adsorption, O_2/N_2 selectivity (including selectivity definition and measurement conditions), and recyclability for representative porous adsorbents and the ZIF materials studied in this work.

Material	Conditions (T (K)/ mixture / P (bar))	Selectivity definition	O_2 Adsorption (mmol g^{-1})	O_2/N_2 selectivity	Recyclability	Ref.
ZIF-8 (Zn:Co = 90:10)-MS	298 / pure-gas / 1	Adsorption ratio (pure-gas)	0.35	2.01	9.9% loss over 3 cycles	This work
ZIF-8-derived Fe-mIM (Zn:Fe = 0:100)-MS	298 / pure-gas / 1	Adsorption ratio (pure-gas)	0.09	2.60	9.6% loss over 3 cycles	
ZIF-8-US	298 / pure-gas / 1	Adsorption ratio (pure-gas)	0.26	1.06	0.5% loss over 3 cycles	
ZIF-62-US	298 / pure-gas / 1	Adsorption ratio (pure-gas)	0.34	1.01	1.3% loss over 3 cycles	
MOF-177	298 / pure-gas / 1	Adsorption ratio (pure-gas)	0.18	~1.8	NA	[14]
UMCM-1	298 / pure-gas / 0.96	Adsorption ratio (pure-gas)	0.23	~1.64	NA	[15]
Zeolite 13X	298 / pure-gas	Adsorption ratio	0.0046	0.0138	NA	[16]

	/ 1.013	(calculated from Langmuir parameters)				
ZIF-8	62.96 / pure gas / 0.01493	NA	22.24	NA	NA	[17]
ZIF-8	308 / pure-gas / 1	Henry's law selectivity (ratio of Henry constants, $K_{<H,O2}/K_{<H,N2}$)	0.087	0.96	NA	[18]
ZIF-62 (crystal)	273 / pure gas / 1	NA	0.00	NA	NA	[19]
a_gZIF-62 (glass)	273 / pure gas / 1	NA	0.067	NA	NA	[19]
(ZIF-8)(ZIF-62)(20/80)	273 / pure gas / 1	NA	0.196	NA	NA	[19]
a_g[$(ZIF\text{-}8)_{0.2}(ZIF\text{-}62)_{0.8}$] (glass)	273 / pure gas / 1	NA	0.071	NA	NA	[19]

References

1. N. Giri, M.G. Del Pópolo, G. Melaugh, R.L. Greenaway, K. Rätzke, T. Koschine, L. Pison, M.F.C. Gomes, A.I. Cooper, S.L. James, *Nature* 2015, **527**, 216.
2. S.L. James, *Adv. Mater.*, 2016, **28**, 5712-5716.
3. R.L. Greenaway, D. Holden, E.G.B. Eden, A. Stephenson, C.W. Yong, M.J. Bennison, T. Hasell, M.E. Briggs, S.L. James, A.I. Cooper, *Chem. Sci.*, 2017, **8**, 2640-2651.
4. M. Taheri, D. Ashok, T. Sen, T.G. Enge, N.K. Verma, A. Tricoli, A. Lowe, D. R. Nisbet, T. Tsuzuki, *Chem. Eng. J.*, 2021, **413**, 127511.
5. M.F. Thorne, M.L.R. Gómez, A.M. Bumstead, S. Li, T.D. Bennett, *Green Chem.*, 2020, **22**, 2505-2512.
6. H. Mahdavi, A. Robin, N.T. Eden, A. Khosravanian, M.M. Sadiq, K. Konstas, S.J.D. Smith, X. Mulet, M.R. Hill, *Langmuir*, 2024, **40**, 17387-17395.
7. H. Mahdavi, H. Zhang, L.K. Macreadie, C.M. Doherty, D. Acharya, S.J.D. Smith, X. Mulet, M.R. Hill, *Nano Res.*, 2022, **15**, 3533-3538.
8. H. Mahdavi, M.M. Sadiq, S.J.D. Smith, X. Mulet, M.R. Hill, *J. Mater. Chem. A*, 2023, **11**, 16846-16853.
9. C.W. Tsai, *Synthesis and absorptive properties of metal-loaded nano-sized zinc zeolitic 2-methlimidazolate frameworks (ZIF-8) with applications in heterogeneous catalysis*, University of the Free State, 2014.
10. J. Cheng, D. Ma, S. Li, W. Qu, D. Wang, *Polymers*, 2020, **12**, 347.
11. G. Khandelwal, N.P. Maria Joseph Raj, S.-J. Kim, *J. Mater. Chem. A*, 2020, **8**, 17817-17825.
12. R.S. Madsen, M. Stepniewska, Y. Yang, A. Qiao, W.M. Winters, C. Zhou, J. König, J.C. Mauro, Y. Yue, *RSC adv.*, 2022, **12**, 10815-10824.
13. S. Cao, T.D. Bennett, D.A. Keen, A.L. Goodwin, A.K. Cheetham, *Chem. Commun.*, 2012, **48**, 7805-7807.
14. Y. Li, R.T. Yang, *Langmuir*, 2007, **23**, 12937-12944.
15. B. Mu, P.M. Schoenecker, K.S. Walton, *J. Phys. Chem. C*, 2010, **114**, 6464-6471.

16. L. Herraiz, E. Palfi, E. Sánchez Fernández, M. Lucquiaud, *Front. Energy Res.*, 2020, **8**, 482708.
17. B. Russell, J. Villaroel, K. Sapag, A.D. Migone, *J. Phys. Chem. C*, 2014, **118**, 28603-28608.
18. C. Zhang, R.P. Lively, K. Zhang, J.R. Johnson, O. Karvan, W.J. Koros, *J. Phys. Chem. Lett.*, 2012, **3**, 2130-2134.
19. L. Longley, S.M. Collins, S. Li, G.J. Smales, I. Erucar, A. Qiao, J. Hou, C.M. Doherty, A.W. Thornton, A.J. Hill, *Chem. Sci.*, 2019, **10**, 3592-3601.